

## §4 200-MeV Linac

### 4.1 Introduction

A 200-MeV proton linear accelerator for the JHF has been designed [1]. It was done on the basis of the accumulated knowledge of construction and operation of the 20-MeV linac at KEK since 1974, the energy extension up to 40 MeV in 1985, research and development of a high-energy, high-intensity proton linac for JHP since 1987 [2] and a large amount of advances in beam-dynamics issues and accelerating structures during past three decades of years in the world. The main features of the requirements for the linac are a high-peak current, a high-average current and a high-duty factor. A peak current of 30 mA ( $H^-$  ions) of 500  $\mu$ sec pulse duration will be accelerated at a repetition rate of 25 Hz. The expected average current will be 200  $\mu$ A at the beginning, and nearly 1 mA in the future. These parameters strongly require the best ability of the total system as well as each device of the linac. In addition, since it is to be used as an injector into the following 3-GeV rapid-cycle synchrotron, supplying beams for many kinds of scientific studies, stable operation with the required beam quality during many years is the most important and necessary character of the linac. In order to construct and operate the linac with such a high quality, the design concept is crucially important. Also, details concerning the design and construction of each accelerator components are important. They would exhibit their best ability if they were to be used according to an correct scenario. Therefore, the final design was determined not only based on the results of a beam-dynamics calculation, but also by careful studies of the accelerating structures, rf devices, and tuning and operation methods.

The linac consists of a 3-MeV radio-frequency quadrupole linac (RFQ), a 50-MeV drift tube linac (DTL) and a 200-MeV separated-type drift tube linac (SDTL)[3]. A frequency of 324 MHz has been chosen for all of the rf structures. A future upgrade plan up to 400 MeV is also considered, in which annular-coupled structures (ACS) of 972 MHz are used in an energy range of above 150 or 200 MeV. There are three distinct features in the design.

The first is its stable operation with high performance for a beam-loss problem during acceleration. It can be achieved firstly by adopting SDTL for a medium energy structure. The space-charge effects in SDTL decreases compared with those in CCL in an accelerator complex (DTL and CCL) with the same transition energy (section 4.2.3). Secondly, the longitudinal transition at a rather high-energy range decreases the effects of nonlinear problems related to acceleration in the CCL. Thirdly, the coupled envelope equations and the equipartitioning theory are used for the

---

\* For section 4.1 to 4.3, serial numbers are used for figures, pages, tables and references . The reference list is added after section 4.3.16.

---

focusing design, resulting in a smaller amount of emittance growth in longitudinal phase space and a smaller ratio of halo formation (section 4.3.8). Finally, up to an energy of 200 MeV, there is no longitudinal transition, which often causes beam losses in the high-energy accelerating part.

The second is its total high shunt impedances. The adoption of the SDTL structure improves both the effective shunt impedance and difficulties in fabricating drift tubes with focusing magnets.

The third is an adoption of klystrons for rf power sources for all of the accelerating structures, resulting in more reliable and easy-handling rf systems.

## 4.2 Basic concept

### 4.2.1 Requirements

The required main parameters for the JHF proton linac are listed in Table 4.1. The construction plan of the linac consists of two stages. In the first stage, a linac of required minimum ability, which can satisfy the injection-beam parameters of the following ring, will be constructed. An upgrade of the linac is being planned from the beginning, and will be gradually performed in order to increase the average beam current based on the accumulated experience of beam acceleration during operation. Negative hydrogens, instead of protons, will be accelerated because of the requirement from the injection scheme into the following ring. This imposes severe restrictions on the beam properties from the ion source, and characterizes the total linac system, since a rather lower peak beam current and a longer pulse length are assumed for an  $H^-$  beam compared with proton acceleration.

An output energy of 200 MeV is required in the first stage of construction. An upgraded energy of 400 MeV is planned for the future. A peak current of 30 mA with a pulse length of 500  $\mu$ sec at a repetition rate of 25 Hz is required in the first stage of construction. There is a future plan to have a peak current of 60 mA, a pulse length of 500  $\mu$ sec and a repetition rate of 50 Hz. The energy spread of the output beam can be controlled to meet the requirements by using a debuncher cavity located a few tens of meters downstream of the exit of the linac.

In order to reduce beam losses after injection into the ring, a fast beam chopper in a low energy region is required. The required time structure of the beam is shown in Fig.4.1. Fast rising and falling times in a pulsed deflecting field are required from the viewpoint of beam losses along the accelerator, since a fraction of the beam during rising and falling times becomes unstable. If beam losses of about 1% along the linac is allowed, the maximum allowable number of unstable micro bunch during a chopping period of 500 nsec is two. It means that the required rising and falling times are about 3 nsec, corresponding to an rf period of 324 MHz.

The total length of the linac imposes an important boundary condition on the design of the total system. The available length of 200 m for the maximum output energy of 400 MeV requires an

Table 1 Required main parameters of the linac.

	Initial requirement	Final goal	
Particles	$H^-$	$H^-$	
Output energy	200	400	MeV
Peak current	30	60	mA
Beam width	500	500	$\mu\text{sec}$
Repetition rate	25	50	Hz
Average current	200	800	$\mu\text{A}$
Length	<150	~220	m
Momentum spread	$\pm 0.1$	$\pm 0.1$	%

average accelerating energy gain of 2 MeV/m, which seems to be rather high compared with those for conventional accelerators; the LAMPF value is 1 MeV/m.

Finally, the other important requirement, which is not listed in the Table 4.1, is to achieve stable operation with minimum beam losses in the acceleration of the required current. Although it is difficult to estimate these properties in terms of the figures, our machine should always be designed, constructed, commissioned and tuned from these points of view.

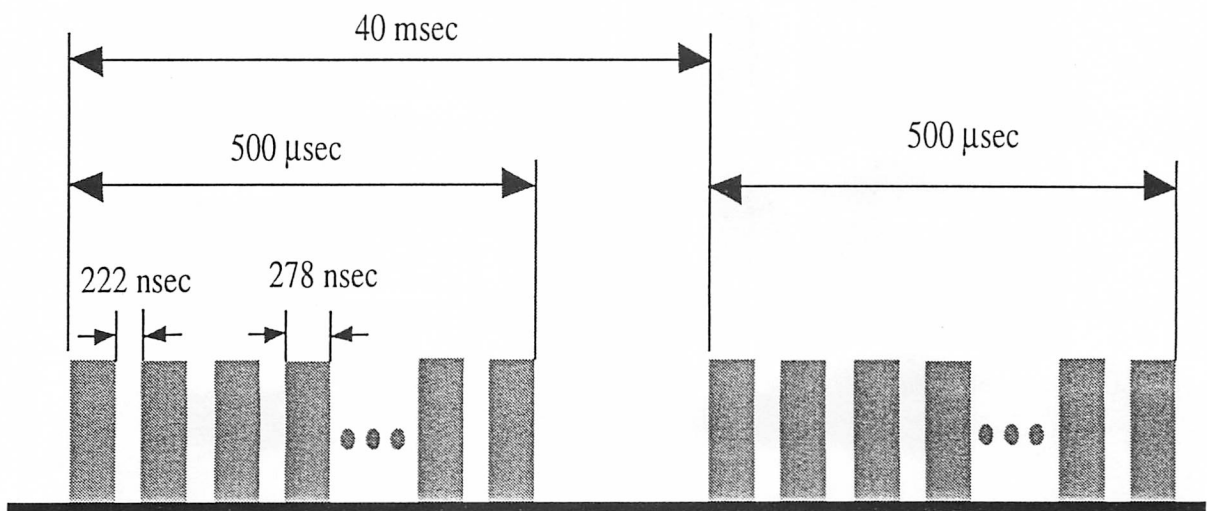


Fig. 4.1 Required time structure of the bunch. A pulse length is 500  $\mu\text{sec}$ . A repetition rate is 25 Hz.

## 4.2.2 Design criteria

Within the framework of satisfying the requirements, our criteria for designing of the linac are as follows:

### 1) Stable operation with minimum beam losses

The JHF linac should be designed and constructed with appropriate margins for beam losses in order to achieve a stable and reliable operation of the total system, including the accelerating structure, rf power supply, water-cooling system, vacuum system and monitor and control system. An accurate beam-dynamics simulation code, including both an accurate electromagnetic field distribution in the acceleration process and a direct three-dimensional space-charge calculation, is used for determining the main parameters of the linac from the viewpoints of not only the rms properties of the beam, but also the behavior of the halo-like particles around the core-part of the beam. Focusing along the linac is performed based upon the theory of the coupled envelope equations as well as equipartitioning theory. It is a useful method from the viewpoints of obtaining a good beam qualities with the space-charge effects and tuning the emittance growth in the transverse and longitudinal phase spaces (section 4.3.8). Here, a beam with balanced properties, between the core and halo part, and between the transverse and longitudinal qualities, is called a good one.

### 2) Easy tuning for varied peak currents

One of the important problems in a high-intensity linac is to establish an effective tuning method for various peak beam currents, since the beam-loss problem often becomes serious when the peak current increases. Therefore, it is required to tune the transverse focusing forces freely for all rf structures in order to compensate for any space-charge effects, which in turn determine the highest possible frequencies for the DTL structure. In order to satisfy the requirements, beam diagnostics systems, carefully prepared along the linac, are crucial. Moreover, in order to obtain reliable beam data which can be compared with the calculated results, it is also crucial to construct accelerating structures and to align them within the required accuracy on the basis of the calculation. It is thus pointed out that it is important to understand the fact that the accumulation of each part of the linac, accurately designed and fabricated, can make the linac reliable and stable.

### 3) Positive adoption of new ideas and devices

A long time has passed since the first-generation high-energy proton linacs were constructed. During this long period, many new ideas for proton linacs were proposed and tested. Although many of

them were dismissed, some proved to be valid for the future linac technology. Therefore, it is a reasonable way to take these new ideas and devices into our design positively.

#### 4) Easy maintenance after construction

The accelerator will supply beams for various scientific research groups for more than ten years. During the long-term operation, many elaborate efforts to maintain and improve the ability of the linac will be required. Thus, the ease of maintenance and modifications should be taken into account during the first design. Although it is difficult to represent these characteristics by figures, the design should be performed on the basis of this criterion.

#### 5) Minimum cost

Everyone knows the importance of low-cost construction. However, cost estimations have difficulties in the sense that each designer sets his own boundary on the total-cost estimation. Therefore, it could be possible to construct accelerating structures with minimum cost and with maximum cost for future improvements and modifications. Generally speaking of accelerating structures, although it is possible to improve one of the rf properties greatly, it usually sacrifices other properties, which become serious problem in some cases. Therefore, more careful studies are required whenever a new idea is extremely superior concerning one of the properties. Thus, our cost optimization should be performed based upon the following criteria:

- 1) a simple accelerator structure, both in rf properties and mechanical structure, is desirable, since it leads to reliable and stable operation with the total minimum cost finally,
- 2) including not only the initial and directly required cost, but also the expected future costs for both maintenance and improvements.

### 4.2.3 Design of the linac

According to the criteria mentioned above, a 200-MeV proton linear accelerator has been designed. It consists of a 3-MeV RFQ, a 50-MeV DTL and a 200-MeV SDTL. A future upgrade plan up to 400 MeV is also included, in which a 972-MHz ACS are used in an energy range of above 150 or 200 MeV. The design is summarized in Table 4.2 and shown in Fig. 4.2. The features of the design are as follows:

1. a frequency of 324 MHz has been chosen for all of the rf structures up to 200 MeV, resulting in no longitudinal transition and suppression of the space-charge effects,
2. an SDTL has been chosen in an energy range from 50 to 200 MeV, resulting in the higher effective shunt impedance,
3. a 3-MeV RFQ has been chosen, resulting in an adoption of electroquadrupole magnets for the

following DTL with sufficient focusing forces,

4. a transition energy of 150 or 200 MeV from the SDTL to the ACS has been selected, and
5. the klystrons are used for all of the accelerating structures.

The main procedures for the final design above mentioned are as follows (details are described in ref. [1]):

1. although beam qualities from all DTL configuration from 3 to 200 MeV is best, its rf-power efficiency and construction cost are not very well,
2. a transition in an operating frequency at an intermediate energy range is not desirable so long as an output energy is less than 200 MeV, since beam qualities become worse, the total rf-power efficiency is not high and cost performance regarding two kinds of rf power sources is not good.
3. although beam qualities are not better than those in all DTL configuration, they satisfy the requirements, and moreover, the final design with an output energy of 400 MeV is superior in rf efficiency and cost performance to any other schemes.

One of the design characteristics is its stable operation with high performance for a beam-loss problem during acceleration. There are three reasons for the above mentioned character:

1. First, it can be achieved by adopting an SDTL for a medium energy structure. Here, the frequency of SDTL is the same as that of DTL. Considering a complex of DTL, SDTL and CCL (coupled cavity linac) of a multiplied frequency, there is a transverse transition from DTL to SDTL and a longitudinal (frequency) transition from SDTL to CCL. On the contrary, both the transverse and longitudinal transitions occur at the same place for a complex of DTL and CCL. It is normally considered that the rate of phase damping in CCL is larger than that in SDTL because of a difference in energy-dependence of the transit time factor. Therefore, the volume of the bunch in SDTL is larger than that in the CCL, assuming that the same transition energy from DTL. Thus, the space-charge effects in SDTL is weaker than that in CCL. In addition, a longitudinal transition in a complex of DTL, SDTL and CCL occurs at a rather higher energy (150 or 200 MeV). Therefore, the bunch length of the SDTL output beam is sufficiently short that the effects of nonlinear problems related to acceleration in the CCL decreases in comparison with a complex of DTL and CCL. The characteristics mentioned above were confirmed using an accurate beam-dynamics simulation code [4], including both an accurate electromagnetic field distribution in the acceleration process and an direct three-dimensional space-charge calculation.
2. Second, the equipartitioning focusing method is used, resulting in three features in beam behavior as follows. First, a less amount of emittance growth in longitudinal phase space can be expected (section 4.3.8), compared with that in a constant transverse phase advance focusing. Second, a smaller ratio of halo formation can be expected (section 4.3.8). Third, a transverse rms beam size does not change abruptly at the transition from DTL and SDTL,

Table 4.2 Parameters of the JHF 200-MeV proton linac (DTL and SDTL).

	DTL	SDTL	
Frequency	324	324	MHz
Injection energy	3.0	50.1	MeV
Output energy	50.1	200.0	MeV
Length (structure only)	27.0	65.8	m
Length (including drift space)	28.5	92.3	m
Number of tank	3	31	
Number of klystron	3	14	
Rf driving power	3.9	16.7	MW
Total rf power (30 mA)	5.3	21.2	MW
Total length		122.2	m
Total power (30 mA)		26.6	MW
Peak current		30	mA
Beam width		500	$\mu$ sec
Repetition rate		25	Hz
Average current		200	$\mu$ A
chopping ratio	~0.56		

### JHF 200-MeV PROTON LINAC

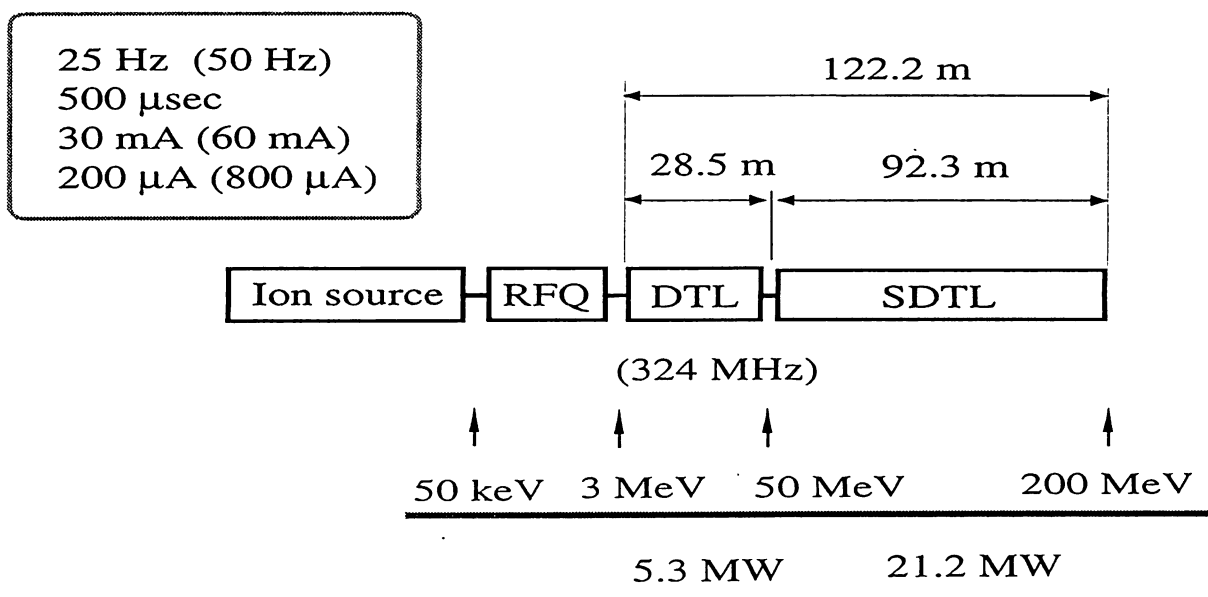


Fig. 4.2 Schematic view of the JHF 200-MeV proton linear accelerator.

since the rms beam size becomes large at the end of DTL.

3. Third, a sufficiently large longitudinal focusing force at the DTL injection point, compared with the transverse focusing force, is achieved by selecting a rather high accelerating field for the DTL injection point (section 4.3.9).

## 4.3 Beam dynamics

### 4.3.1 Introduction

The purpose of the beam dynamics calculation is to find the optimum parameters of linac from the viewpoints of both the rms properties of the output beam and behaviors of the halo-like particles around the core part of the beam. It is also important and stressed that the obtained parameters are rational from the viewpoints of fabrication and operation. We are apt to forget these points since the devices with higher ability and efficiency is usually more attractive.

### 4.3.2 Choice of the operating frequency

In the frame work of our peak beam current of about 30 mA ( about 60 mA in the future), our major concern is how to obtain a beam of good quality without beam losses, instead of finding the maximum current in the linac. Therefore, the emittance growth as well as a beam-halo formation in the both transverse and longitudinal motion along the linac becomes a main beam-dynamics issue. A choice of the operating frequency is closely related to the above mentioned issues via space-charge effects. Comparison of the accelerator parameters for various operating frequencies are summarized in Tables 4.3 and 4.4, calculated based on the assumptions as follows:

1. a zero-current transverse phase advance of 60 degrees with FODO focusing scheme,
2. an optimum radius of beam hole varies in proportion to square-root of wavelength, and
3. the same accelerating field for all frequencies, assuming a relatively high duty factor linac, where the accelerating field is mainly determined by rf power dissipation in the structure.

A frequency of 324 MHz is selected for the following reasons:

1. the space-charge effects are greatly reduced compared with a conventional frequency of 200 MHz,
2. the electroquadrupole magnets with sufficiently strong focusing strength for drift tubes are possible on the assumption of a 3-MeV RFQ,
3. a 3-MeV RFQ of a single tank is possible,
4. a klystron is possible with some modifications from that at a frequency of 350 MHz, and
5. an ACS for a high- $\beta$  structure is possible assuming a frequency multiplication factor of three.

Table 4.3 Accelerator parameters for various operating frequencies.

Frequency	201	300	324	350	432	MHz
Emittance(90%)	0.15	0.15	0.15	0.15	0.15	$\pi$ cm·mrad (normalized)
Eacc	2	2	2	2	2	MV/m
Beam radius	2.45	1.85	1.77	1.69	1.47	mm
$\Delta\phi$	6.4	8.5	9.0	9.6	11.6	degree
B'	43.3	96.5	112.6	131.4	200.2	T/m
$\sigma_x^0$	60	60	60	60	60	degree
$\sigma_x$	42.4	50.0	51.1	52.2	54.4	degree
$\sigma_x/\sigma_x^0$	0.71	0.83	0.85	0.87	0.91	
$\mu_t$	0.50	0.31	0.27	0.24	0.18	
EGF	5.0	2.3	1.9	1.6	1.1	%

EGF: emittance growth factor due to the field energy of the bunch of Gaussian distribution.

Table 4.4 Parameters related to transverse focusing vs. frequencies in a 3-MeV injection into the DTL. FODO focusing scheme with a phase advance of 60 degrees is assumed.

Frequency	Cell length	$\beta_{\max}$	Bore radius	Q-mag radius	B'	Bsurface
MHz	mm	m	mm	mm	T/m	kG
201	119.0	0.395	9.37	11.37	43.4	4.94
300	79.7	0.264	7.67	9.67	96.7	9.35
324	73.8	0.245	7.38	9.38	112.7	10.6
350	68.3	0.227	7.10	9.10	131.6	12.0
432	55.4	0.184	6.39	8.39	200.4	16.8

### 4.3.3 Beams for the input of simulations

It was reported [5] that the 3-MeV, 432-MHz RFQ at the test stand at KEK accelerates a 13.2-mA beam with a transmission efficiency of 82.5% and with an emittance growth ratio of 34%: a 90% transverse emittance of  $0.55 \pi\text{mm.mrad}$  has been obtained. However, we have not yet had the accurate information on characteristics of a 30-mA, 3-MeV beam from an RFQ of 324 MHz. Therefore, we have prepared two kinds of injection beams of different emittances (Table 4.5) in order to consider the beam behavior from a broad perspective. The injection particles are generated randomly in a six-dimensional ellipse.

### 4.3.4 The medium energy beam-transport line (MEBT)

#### 4.3.4.1 Design of the MEBT

The MEBT plays dual roles in the JHF linac : one is to match the beam from the RFQ with the DTL acceptance in 6-D phase spaces; another is to chop the macropulse for beam injection to the ring. To accomplish the two tasks, the beam line consists of quadrupoles, bunchers and choppers.

TRACE 3-D [6] is applied in the beam line design. In order to describe the beam deflection behavior, TRACE 3-D has been modified to include a new element: RF deflector. This subroutine follows the reference particle offset by the transverse electric and magnetic fields of RF deflector, and meanwhile transports the beam with longitudinal coupling of different phase of the beam bunch to the deflecting angle, which increases the emittance in the deflecting plane. MAFIA [7] is used to design the deflector cavity and to provide the field distribution data for TRACE 3-D. The amplitude distribution of the deflecting electromagnetic field along beam line is read into TRACE 3-D for field generation. In this way, the fringe E and B fields of the electrode can be taken into account, which partially compensates the deflecting efficiency. In the MEBT design, unchopped beam quality conservation and high deflection efficiency for RF deflector are always pursued.

As a result, the MEBT is proposed with the total length of about 2.3 m, as shown in Fig. 4.3. The

Table 4.5 Two kinds of injection beams used for the simulations.

	Type A	Type B
rms transverse emittance	0.187	0.375 $\pi\text{mm.mrad}$
rms longitudinal emittance	0.133	0.266 $\pi\text{MeV.deg}$

up-left plots in the figure represent the input beam phase space for Type A injection beam in Table 4.5. In the beam profile plot at the bottom of the figure, the beam-centroid offset in x direction by RFD is depicted by the dark cross line. The beam dump will be positioned at the element 18 for chopped beam. The separation between chopped and unchopped beam is 6.6 mm at the dump, as each of the two RF deflectors has deflecting field of 1.4 MV/m. This large separation is contributed from not only the two RF deflectors, but also the fourth quadrupole, element 16. The deflection is initiated by the two RF deflectors with angle of 5.3 mrad for each and then amplified three times by the quadrupole. Downstream the quadrupole, the deflection angle becomes 33.1 mrad. Owing to this reason, the RF deflector requires no much RF power for adequate deflection. The first three Q magnets can be adjusted for a small beam profile in x direction at the fourth Q magnet, aimed at a little defocusing for beam envelope but larger defocusing for the beam centroid. And they should also keep the beam envelope not too large in y direction. The final four Q magnets can be adjusted for transverse beam matching to DTL acceptance. Two bunchers, denoted as G in the figure, can achieve perfect matching in longitudinal direction. The matched beam phase spaces are shown in the up-right plots of the figure.

Beam emittance growth for the unchopped beam is studied by means of PARMILA [8] simulation with 10,000 particles. Figure 4.4 shows the RMS emittance variation versus the element of the beam line. The beam has an RMS emittance growth of 5%, 18% and 11% in x, y, z directions, respectively.

The same beam line can also be used for Type B with beam current of 60 mA and double initial emittances in each direction. Only very little adjustment is necessary for large deflection and matching. For Type B, higher deflecting field of 1.8 MV/m is needed to generate 5.9 mm separation, due to the fact that the beam envelope is larger than that in Type A. PARMILA run shows the emittance increases 4%, 16%, 16% in x, y, z directions, respectively.

In the MEBT, sufficient space is available for beam diagnostics and mechanical connection of the transport elements. It is necessary to measure beam emittance during a long term operation. To do this, the drift space of element 17 is long enough for the insertion of a bending magnet, which leads the beam to a diagnostics beam line. The parameters of MEBT are listed in Table 4.5.4 and plotted in Fig. 4.5.22 in section 4.5.6.

#### 4.3.4.2 Chopper Design

RF deflector is very compact and can provide a high deflecting field. Owing to these characteristics, an adequate deflection can be obtained in such a short beam line. An RF deflector of 432 MHz for JHP was designed and a test model was made [9]. In the present MEBT, RF deflector of 324 MHz has been designed. A lot of MAFIA runs were conducted for optimization of the cavity geometry. Because the required RF power  $P$  is inversely proportional to  $R_s/Q_0$ , with  $R_s$  being transverse

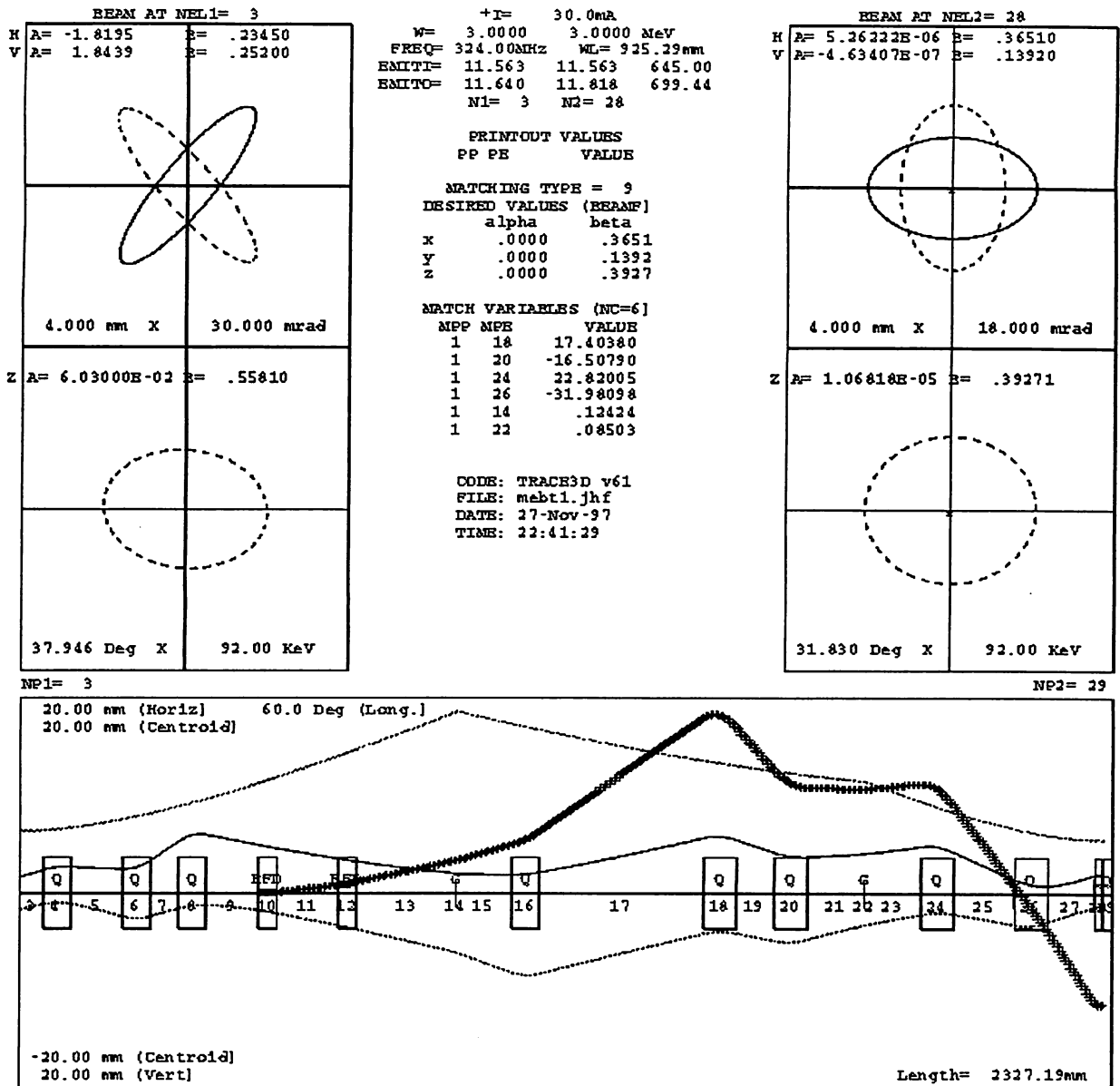


Fig. 4.3 TRACE 3-D output of the MEFT for Type A. In the up-left are the input beam phase spaces and in the up-right is the matched beam with DTL. The bottom are the beam profiles in z, x and y directions, respectively. The dark line traces the beam-centroid offset by the two RFDs.

shunt impedance and  $Q_0$  being unloaded quality factor:

$$P = \frac{V^2}{\omega_0 \tau \left( \frac{R_s}{Q_0} \right)}$$

for a rising time  $\tau$  and certain deflecting voltage  $V$ , the geometry should have  $R_s/Q_0$  as large as possible for low power and short rising time. A cavity geometry is found with  $R_s = 4.7 \text{ M}\Omega$ ,  $Q_0 =$

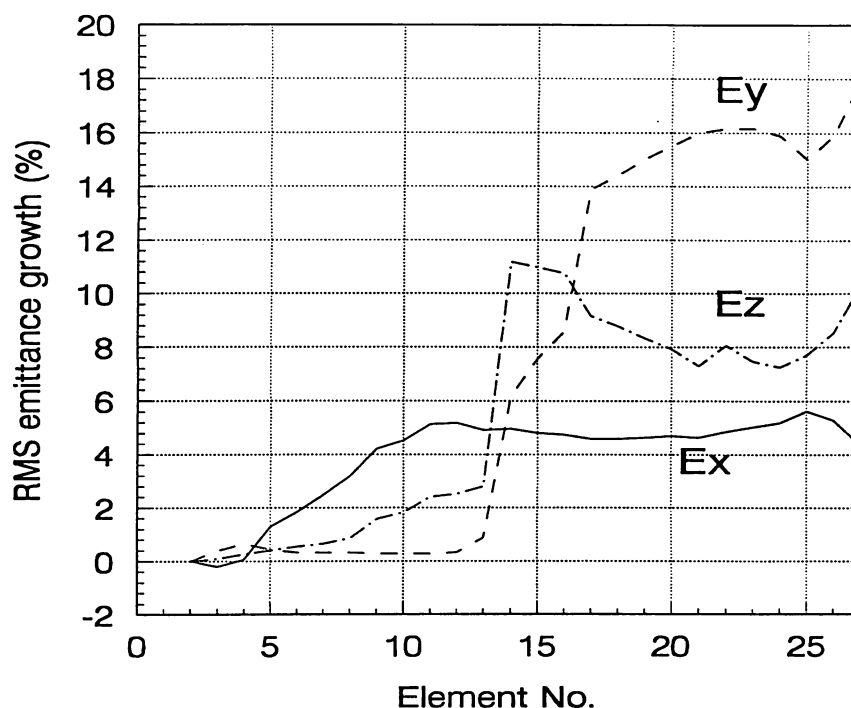


Fig.4.4. RMS emittance growth vs. the beam line elements

10,650. To get a rising time less than 10 ns, the cavity should have the loaded  $Q_L$  about 10. Therefore the required RF power for the RF deflector in Fig.4.3 is reasonably 21 kW. If higher power is fed, the rising time can be reduced more while keeping the same deflecting voltage. Of course, the capability of the coupler for larger  $Q_L$  needs further study. In this cavity, the deflecting electrode length is shorter than  $\beta\lambda/2$  in beam passing direction. It gives the benefits in two folds: an increase in  $R_s/Q_0$ ; the fringe field with high amplitude near the electrodes is in phase with that of the beam, making use of the fringe field positively. The field distribution in the cavity is given in Fig. 4.5(a), which is used for the calculation in Fig.4.3.

The dependence of the separation between chopped and unchopped beams at the beam dump on the RF power of the RF deflector is almost linear, as shown in Fig.4.5(b). Generally, the deflection is scaled to the square root of the power. But in this design, the deflection at beam dump is enlarged by the quadrupole and hence a linear relation appears.

#### 4.3.4.3 Analysis on the unstable particles

It is very crucial for the chopper to have the unstable particles as few as possible during RF rising and falling time. It is noted that the beam will not totally become unstable particles during transient time because the scraper at element 18 in Fig.4.3 is capable to stop some part of the particles in a

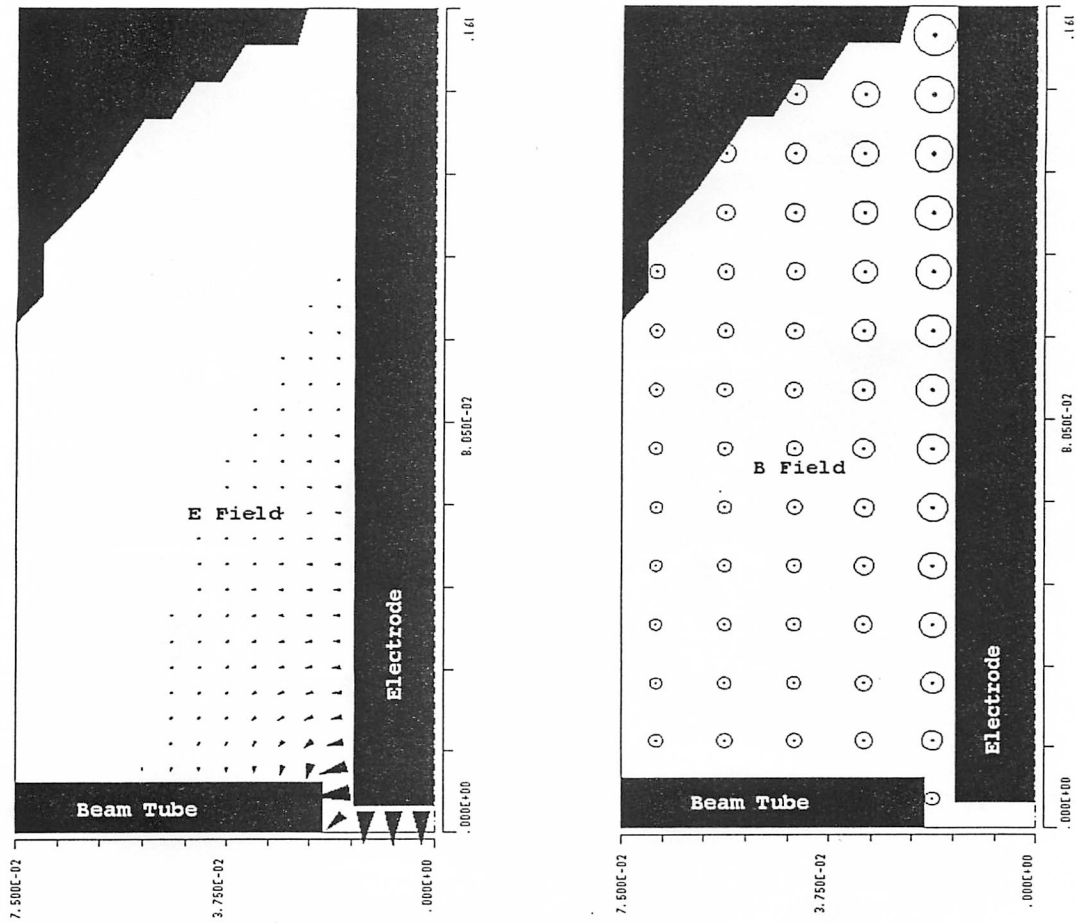


Fig.4.5(a) E and B field distribution in half of the RF deflector

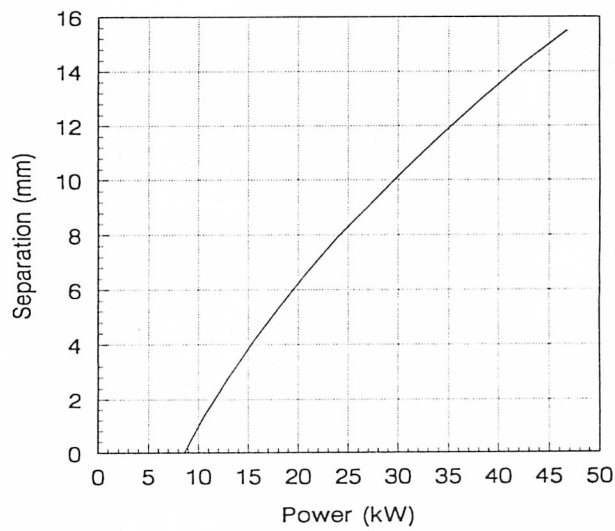


Fig.4.5(b) The beam separation vs. the required power to the RF deflectors in Fig.3.4.

beam when RFD field is not at its full amplitude. To investigate the unstable particle during transient time, PARMILA simulations with 5000 particles in uniform initial phase space are conducted. A particle scraper with width of 10 mm in x direction is positioned at element 18. As the RFD field increases toward its full value 1.4 MV/m, the unstopped particle ratio in a bunch declines, as shown in Fig.4.6(a). According to the simulation on transient duration given in Fig.4.7(b), there are four micro-bunches during rising-time and two in falling-time. The bunches meet the field amplitude as denoted by arrows in Fig.4.6(a).

When the field is more than 80% of the full value, the particles are almost totally stopped by the scraper in Fig.4.6(a). On the other hand, as the field is less than 30%, the unstopped beam is still within the acceptance of the DTL, as shown in Fig.4.6(b) given by TRACE 3-D. So during the field-variation time from 30% to 80% of the full value, the beam will become unstable. But, a part of the beam particles is unstable, because some of them can still be stopped by the scraper.

During rising time there are four bunches. Two of them meet the field at 10% and 85% amplitude. So they will not become unstable beams. The other two bunches meet the field at 40% and 65% amplitude. They partially contribute to the unstable particles. For the bunch at 40% field, the unstable portion is 78% of the bunch particles and for the one at 65% field, the portion becomes 25% of the bunch particle distribution. Therefore, totally the particles in one bunch will become unstable during rising time. In the falling time there is only one bunch, subjected to the field of 50%, after the RF phase is reversed, as described in Fig.6.7(b). The following bunches meet field less than 10% amplitude. So only 58 % of particles in the one bunch will become unstable. Totally during transient times, the particles, corresponding to 1.6 bunches, will become unstable. This means that the equivalent rising/falling time is less than one rf period (3.1 ns) if the rising/falling time is defined as the duration during which the beam becomes unstable. In other words, the ratio of unstable particles to total one is 0.99%.

Although the chopper with RF deflectors shows a good performance according to above calculations, there are still some issues calling for further investigation:

- 1) The errors in DTL subtract the acceptance, and hence the unstable particle fraction may increase;
- 2) Although the beam, kicked by a low deflecting field during transient times, can be accepted into DTL, the beam quality is not good and some particles may experience some nonlinear field in DTL, and then may be lost during acceleration.

This design is characterized with the compactness and high deflection efficiency owing to the application of RF deflector and quadrupole amplification. On the other hand, it requires the RF cavity has a high output coupling coefficient to decrease the unstable particle number. Test research will be conducted on this issue in future.

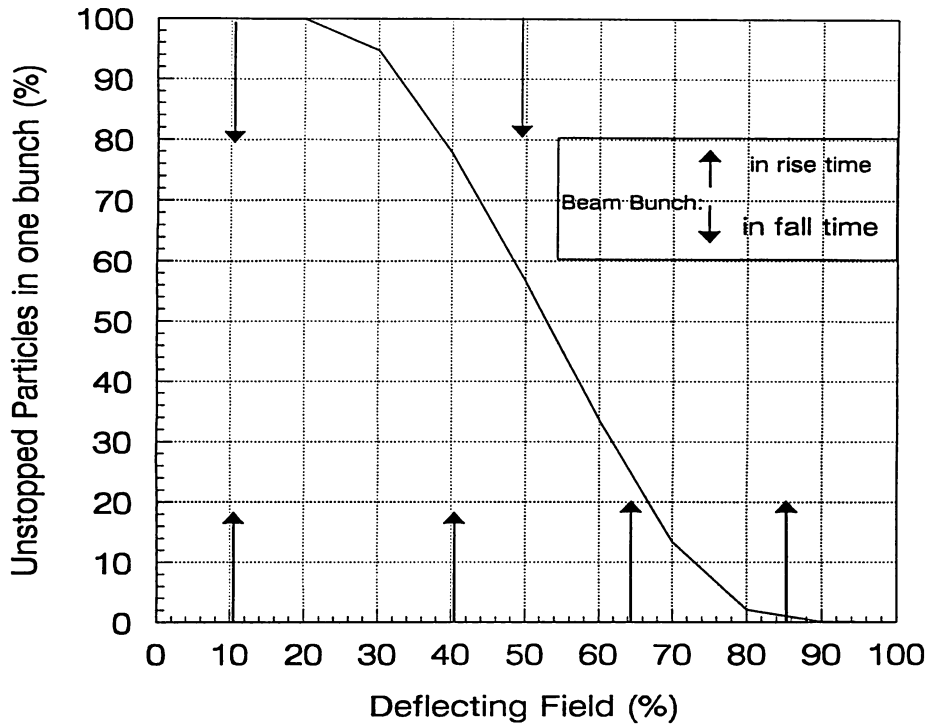


Fig.4.6(a) The unstopped particles ratio in one bunch vs the deflecting field variation, from PARMILA multiparticle simulations. Arrows stand for the bunch distribution during RF rising/falling time.

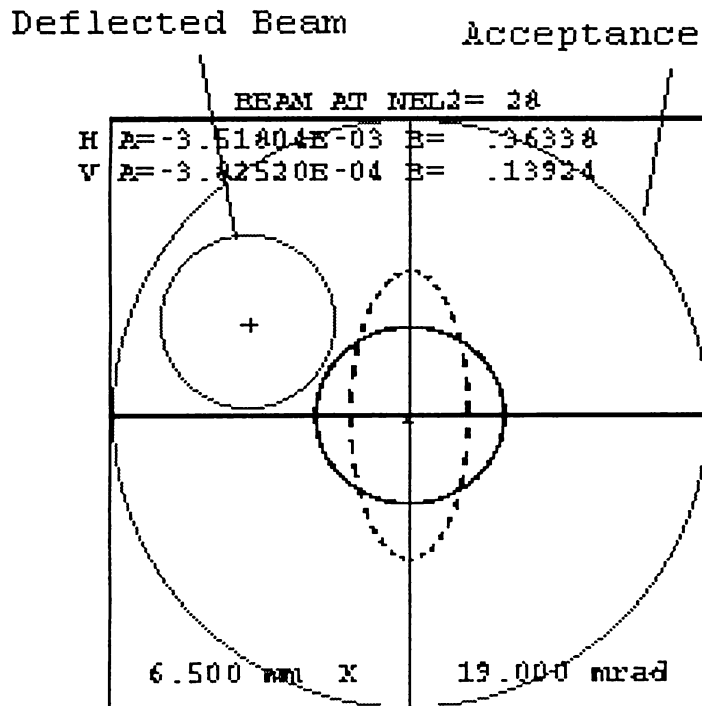


Fig. 4.6(b) Phase space at the entrance of the DTL. The deflected beam is within the acceptance of the DTL when the deflecting field is 30% of the full value.

Behavior of the chopped beams during the transient times were further investigated by beam dynamics simulation with the code LEBT [10] and PARMILA. According to the results shown in Fig. 4.6(a), there are four micro pulses during the rising time and two during the falling time of the deflecting pulse in the RFD. The calculated transmission ratios for the micro bunches through the accelerating system, composed of both the MEBT and the 50-MeV DTL of three tanks, as a function of the electric field in the RFD during transient times, are plotted in Fig. 4.6(c). The results both at the MEBT and DTL exits are presented. Here, two kinds of DTL simulation were performed: one is the matched simulation without scrapers and the other is the matched one with three scrapers: each scraper was set after each DTL tank, at a position of 3 mm from the beam axis in the x-direction. It was shown in the simulation that the unchopped beams were unaffected by these scrapers. The type-A injection beam (30mA) was used in the simulation. An example of the output emittances are shown in Fig. 4.6(d). The results for transmission through the DTL are summarized as follows:

- 1) The transmission ratio for the micro bunch with a 10%-RFD field is more than 97%. Since the deflecting field is small, the output emittance at the DTL exit is nearly the same with that of the unchopped beam, indicating that this pulse is stable.
- 2) The transmission ratios for the micro bunches with the RFD fields of 40 and 50% are 12 and 1%, respectively, when the scrapers are used. There is a possibility that these pulses become unstable after injection into the ring, since the emittances of these pulses are outside the unchopped-pulse emittance at the DTL exit.
- 3) The transmission ratio for the micro bunch with a 65%-RFD field is zero when the scrapers are used.

In conclusion, it was found that very high efficiency of the RFD operation can be achieved by using scrapers along the DTL tanks: a fraction of the unstable transmitted particles through the DTL with the scrapers during transient times was reduced to as small as 0.08% of the total injection beam into the MEBT.

One of the important issues in an rf chopper is how to obtain very fast rising and falling time in order to reduce the number of unsatisfactorily deflected particles during transient duration. An expected rf amplitude in the chopper is shown in Figs. 4.7(a) and 4.7(b). A falling time is improved drastically by using a rapid change in rf phase of the input rf power. A preliminary experiment for producing a high-power rf pulse was performed by using a 201-MHz solid-state power amplifier and a fast rf switch. Figure 4.7(c) shows an rf amplitude of the output power. A peak power level is about 8.5 kW. An improvement of the rising and falling time can be expected since this amplifier was made for a pulse operation with slow rising time.

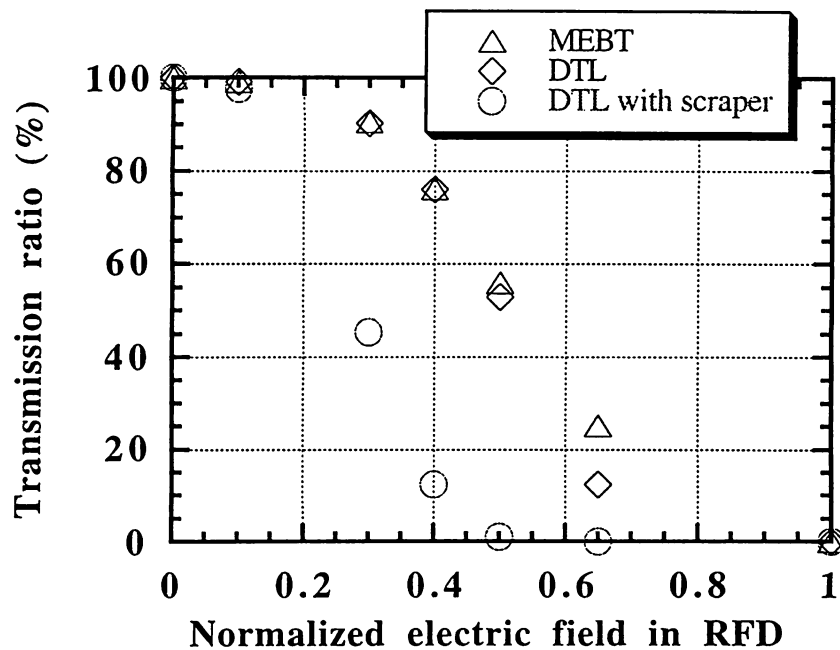


Fig. 4.6(c) Calculated transmission ratios for the micro bunches through the accelerating systems with the MEBT and the 50-MeV DTL, as a function of the electric field in the RFD.

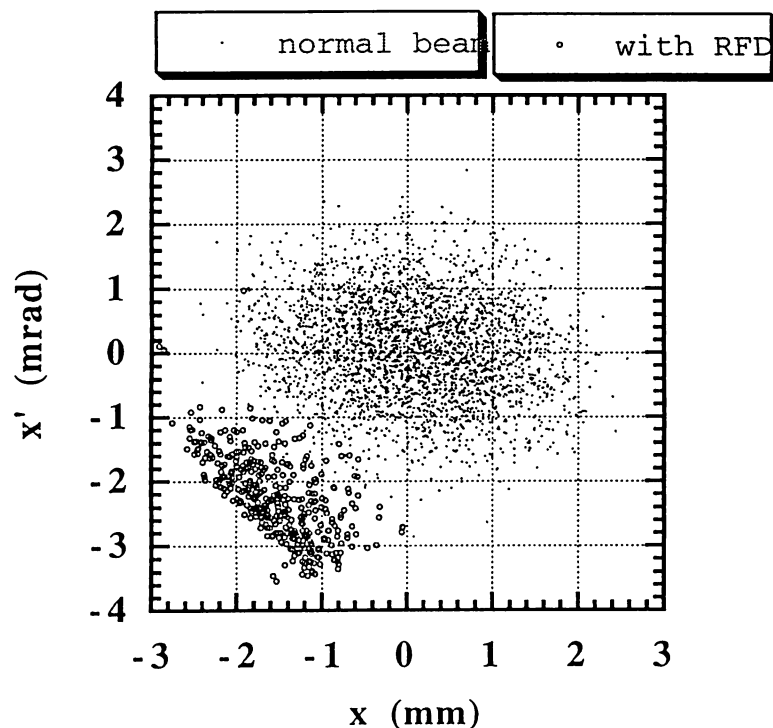


Fig. 4.6(d) Output emittances for the normal-unchopped bunch and the chopped one with a 40%-RFD field at the DTL exit. Two scrapers after DTL tank-1 and tank-2 are used for eliminating the outer part of the chopped bunch. The ratio of number of particles of the chopped bunch is 12.4% of the normal one.

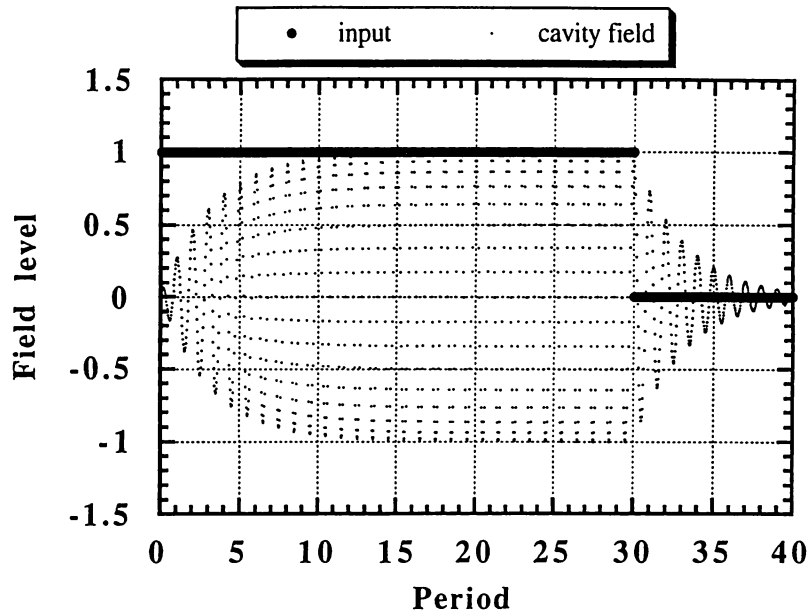


Fig. 4.7(a) Cavity field with a normal driving method. A wider line represents incident field strength.

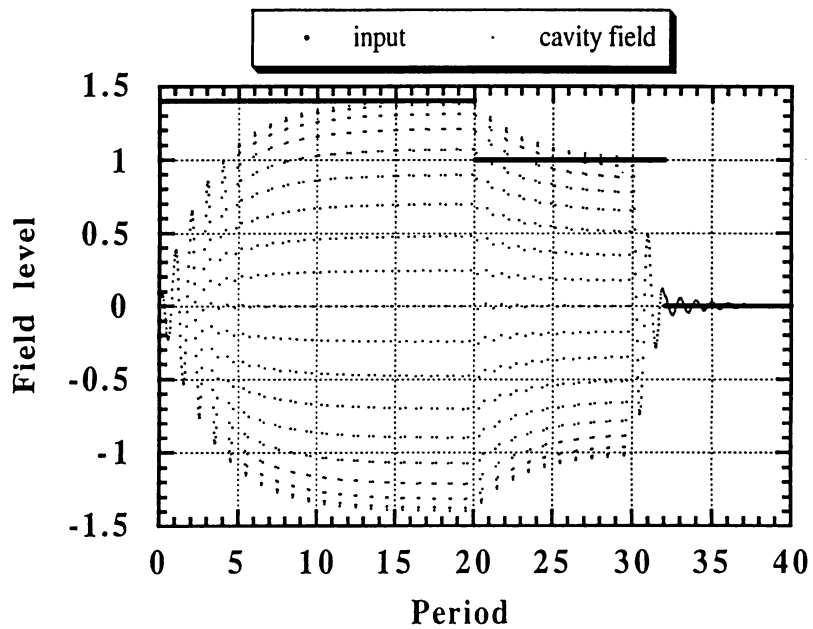


Fig. 4.7(b) Cavity field with an improved method. The initial amplitude ( $E_m$ ) of the incident power is 1.4 times higher. After some time,  $E_m$  is adjusted to 1. A rapid phase shift is added at a timing of turn-off. After some time (at about 33-th periods in this figure), the incident power is turned off.

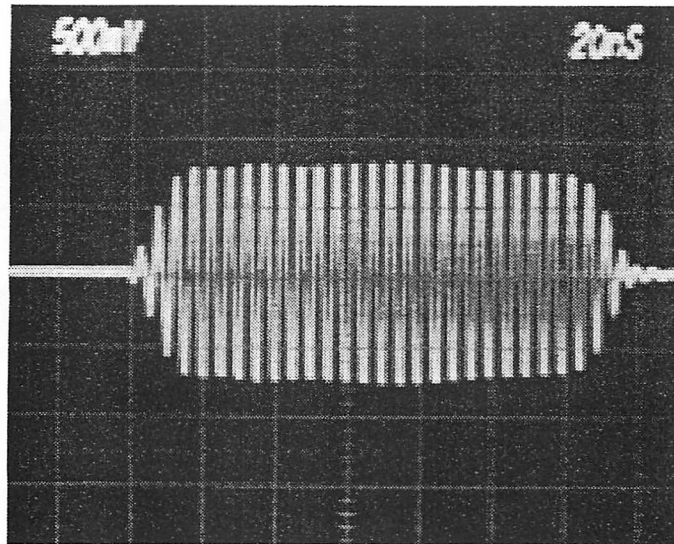


Fig. 4.7(c) Shape of an rf pulse for the chopper cavity, measured in the preliminary experiment at a frequency of 201 MHz. A peak power is about 8.5 kW. 20nsec/div.

#### 4.3.4.4 Buncher

In the MEBT design, the two bunchers should provide effective bunch voltages of  $E_0TL=0.124$  and 0.085 MV for the first and second bunchers, respectively. Two single cavities are designed with the same size for simplicity. According to the beam envelope at the first buncher, a relatively large bore-radius of 15 mm is chosen. The cavity length ( $L$ ) is 160 mm long in the beam passing direction in order to obtain a large shunt impedance. Low Kilpatrick multiplication is wanted to avoid any possible breakdown. So the gap length between noses is 18 mm. SUPERFISH run shows that the cavity can generate the effective voltage for the first buncher with input power of 6.7 kW. The maximum surface electric field is just equal to Kilpatrick limit at 324 MHz.

### 4.3.5 Focusing design

Both the transverse and longitudinal focusing parameters are determined on the basis of equipartitioning theory combined with coupled envelope equations for the bunched beam, written as (refs. [11-13]):

$$k_{x0}^2 a - \frac{3}{2} \frac{Nr_c}{\beta_0^2 \gamma_0^3} \frac{1}{az_m} \left( 1 - \frac{g_0}{2} \frac{a^2}{\gamma_0^2 z_m^2} \right) - \frac{\epsilon_{nx}^2}{\beta_0^2 \gamma_0^2 a^3} = 0,$$

$$k_{z0}^2 z_m - \frac{3}{2} \frac{Nr_c}{\beta_0^2 \gamma_0^5} \frac{g_0}{z_m^2} - \frac{\epsilon_{nz}^2}{\beta_0^2 \gamma_0^6 z_m^3} = 0,$$

$$r_c = \frac{q^2}{4\pi\epsilon_0 mc^2},$$

$$g_0 = 2 \frac{z_m^2}{a^2} M_z.$$

Here,  $k_{x0}$  and  $k_{z0}$  are the zero-current wave numbers for transverse and longitudinal oscillations,  $\epsilon_x$  and  $\epsilon_z$  the rms emittances of the transverse and longitudinal phase spaces,  $a$  and  $z_m$  the radii of the bunch in the transverse and longitudinal directions,  $N$  the number of particles in a bunch,  $M_z$  the ellipsoidal form factor,  $q$  the unit charge,  $\epsilon_0$  the absolute permittivity of free space,  $c$  the velocity of light,  $\beta_0$  the relative velocity and  $\gamma_0$  the relativistic parameter. The wave numbers, including space-charge effects, are written as

$$k_x^2 = k_{x0}^2 - \frac{3}{2} \frac{Nr_c}{\beta_0^2 \gamma_0^3} \frac{1}{a^2 z_m} \left( 1 - \frac{g_0}{2} \frac{a^2}{\gamma_0^2 z_m^2} \right).$$

$$k_z^2 = k_{z0}^2 - \frac{3}{2} \frac{Nr_c}{\beta_0^2 \gamma_0^5} \frac{g_0}{z_m^3}.$$

Therefore, the focusing parameters as well as the beam parameters should be calculated cell by cell using the initial parameters given at the entrance of the linac.

Since it is not easy to vary the accelerating field without any troublesome reactions during operation, the longitudinal focusing strength ( $k_{z0}$ ) is fixed during operation. For the uniformly distributed field, it varies as the energy increases,

$$k_{z0} \propto \frac{1}{(\beta_0 \gamma_0)^{3/2}}.$$

On the contrary, the transverse focusing force varies as

$$k_{x0} \propto \frac{1}{\beta_0}$$

if the zero-current phase advance remains constant along the acceleration. One choice of the variation of the focusing forces is to keep the ratio between the transverse and longitudinal focusing forces constant along the acceleration. In such a case, the transverse focusing force should be decreased along the acceleration in the same manner as the longitudinal force. Then, the transverse beam radius becomes larger than that with the constant phase-advance focusing method. It is also a good choice from the viewpoint of space-charge effects, since the density of the bunch decreases. A demerit of this focusing method is that it requires a larger bore radius. However, from the viewpoint of transitions, an average transverse beam radius varies smoothly from the DTL to the SDTL because of adoption of equipartitioning focusing method in the DTL, although the modulation factor of the envelope becomes larger in the SDTL. In addition, there is no further transition in transverse motion between the SDTL and the CCL.

The injection parameters, related to both the beams and structures, are chosen so that the equipartitioning condition is satisfied. The condition is given by

$$\gamma_0 \frac{\epsilon_{nx}}{\epsilon_{nz}} \frac{z_m}{a} = 1 \quad \text{or} \quad \frac{k_x \epsilon_{nx}}{k_z \epsilon_{nz}} = 1,$$

where the suffix of n means a normalized emittance and  $k_x$  and  $k_z$  are the wave numbers of the transverse and longitudinal phase oscillations with space-charge. Matched and equipartitioning parameters of the injection beam into the DTL are listed in Table 4.6. The main focusing parameters along the DTL are plotted in Figs. 4.8, 4.9 and 4.10. These parameters are typical. In the operation, the focusing parameters should be calculated again according to both the measured injection beam parameters, and carefully adjusted in order to find an optimum quality of the output beam. In such a procedure, the focusing field gradient may be tuned to intermediate values between the results of the equipartitioning focusing method and those of the constant phase focusing one, shown in Fig. 4.11, according to the expected values of emittance growths in both phase spaces.

Table 4.6 Example of matched and equipartitioned parameters of the injection beam into the DTL.

Current	30	60	mA
Beam radius (90%)	1.83	1.98	mm
Beam radius (rms)	0.82	0.89	mm
$\Delta p/p$ (rms)	0.004	0.004	
$\Delta\phi$ (rms)	7.7	9.1	degree
Bunch length (rms)	1.6	1.9	mm
Bunch length (90%)	3.5	4.2	mm
$\varepsilon_{nx}$ (90%)	1.5	1.5	$\pi$ mm-mrad
$\varepsilon_{nz}$ (90%)	2.5	3.0	$\times 10^{-6}$ m
B'	107.4	107.4	T/m
$\sigma_{x0}$	58	58	degree
$\sigma_x$	48	42.7	degree
$\sigma_{z0}$	30	30	degree
$\sigma_z$	21.5	18.1	degree
$\Delta w$ (rms, half)	24	24	keV
$\Delta w$ (90%,half)	53.7	53.7	keV
$\Delta\phi$ (90%,half)	17.2	20.3	degree
Partition parameter	1.15	1.06	

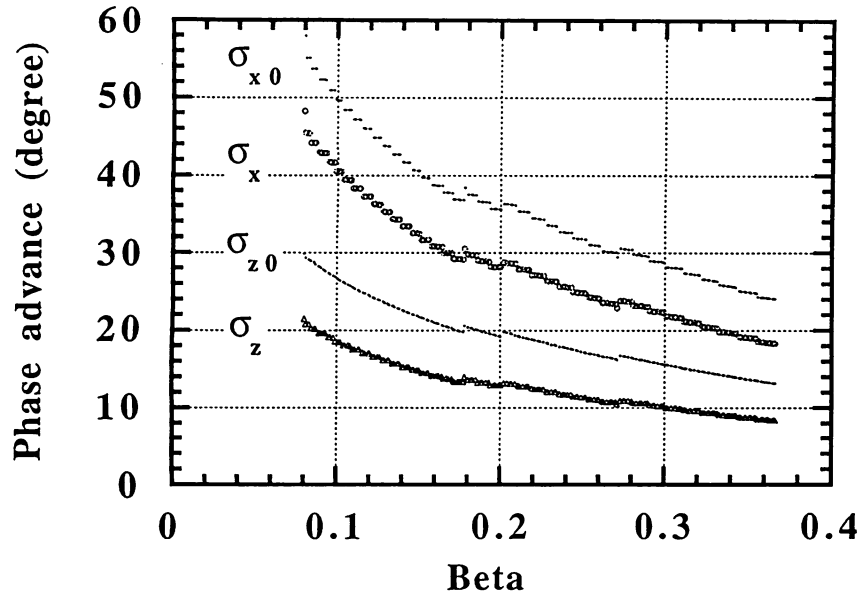


Fig. 4.8 Phase advances in both the transverse and longitudinal phase spaces along the DTL. A peak current of 30 mA is assumed.

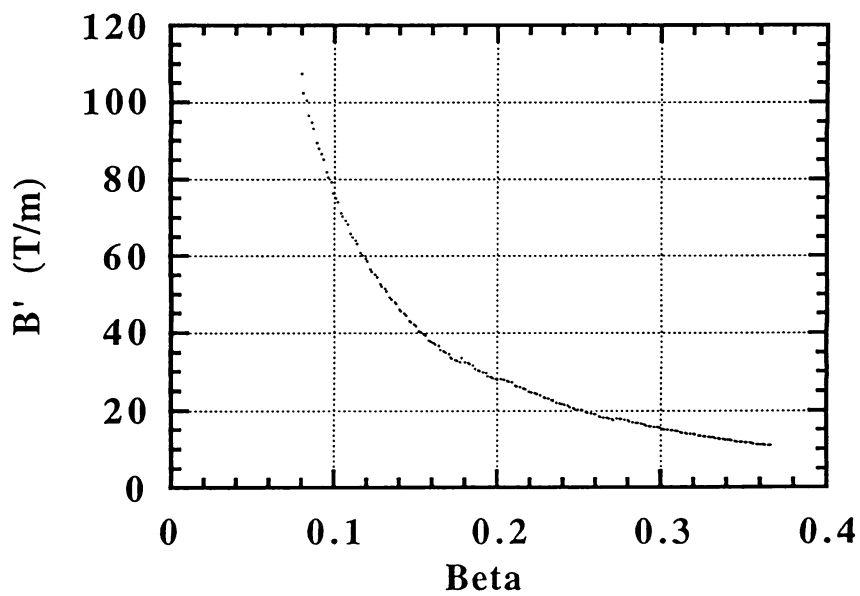


Fig. 4.9 Required magnetic field gradient along the DTL.

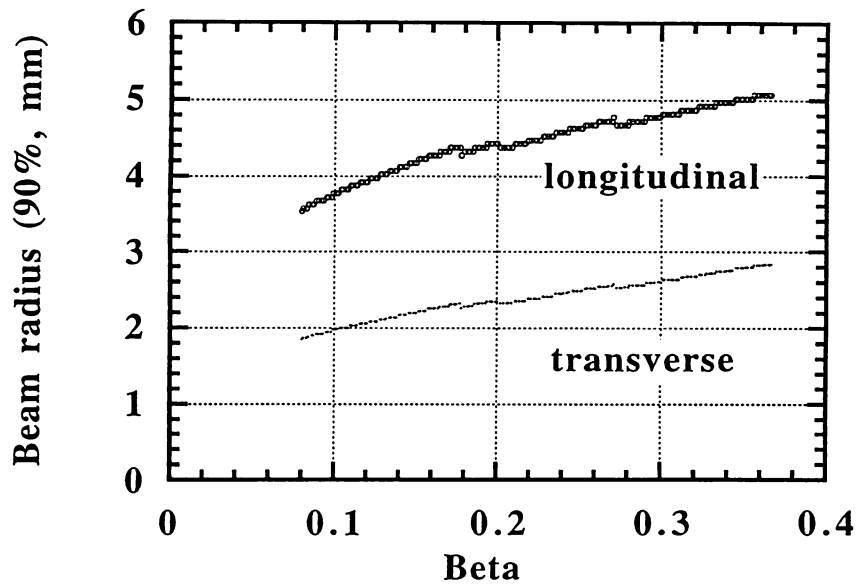


Fig. 4.10 Variation of the beam size along the DTL in the equipartitioning focusing scheme.

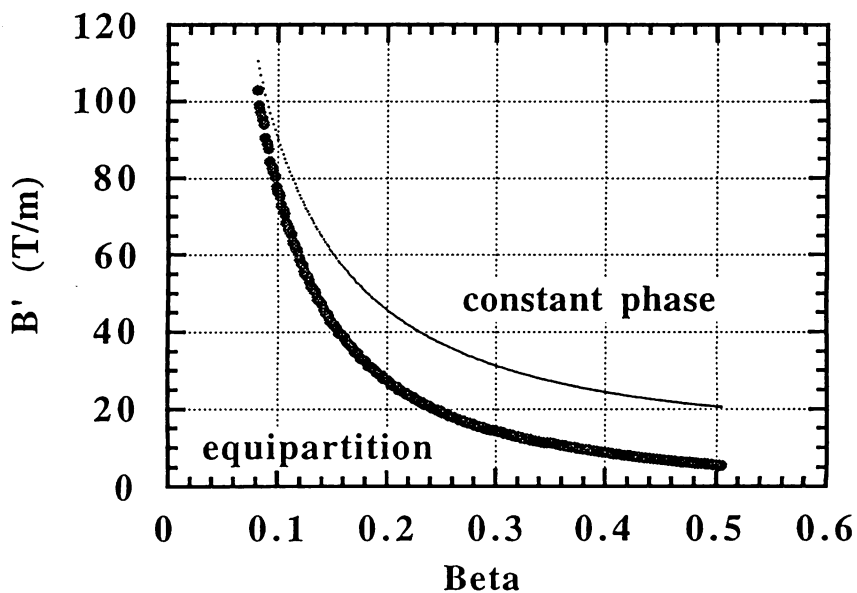


Fig. 4.11 Required magnetic field gradients for both the equipartitioning focusing method and the constant phase advance focusing method.

### 4.3.6 Matching

Matching of the beam parameters to the accelerator ones is one of the most important issue for achieving a good quality of the output beam with smaller emittance growth and beam-halo formation. Therefore, the matching at every stages of transitions should be carefully examined for both freedom of motion. As for the longitudinal matching at the entrance of the DTL, the simulation results indicate that the degradation of the beam quality is not very sensitive to mismatching. Figure 4.12 shows the relative growth of the rms and 99% longitudinal emittances during acceleration from 3 to 148 MeV as a function of a mismatching factor. Here, mismatching factor is defined by a ratio of  $\beta$  (one of the twiss parameters) for the mismatched injection to that for the matched injection. This fact implies that the tolerance for longitudinal matching at the DTL entrance is large. In fact, a mismatching error of 25% in one of the longitudinal twiss parameters ( $\beta$ ) causes additional longitudinal emittance growth of 5% for both the rms and 90% emittances and 20% for 99% emittance for JHF beam parameters. In connection with this point, it should be noted that the effects of ratio of focusing forces between the transverse and longitudinal focusing upon the final beam quality is large in the DTL acceleration [14]. Therefore, it is required not only to consider the matching of the beam in each freedom of motion independently but also to take account of the ratio of focusing forces, both in the transverse and longitudinal motions, along the DTL acceleration.

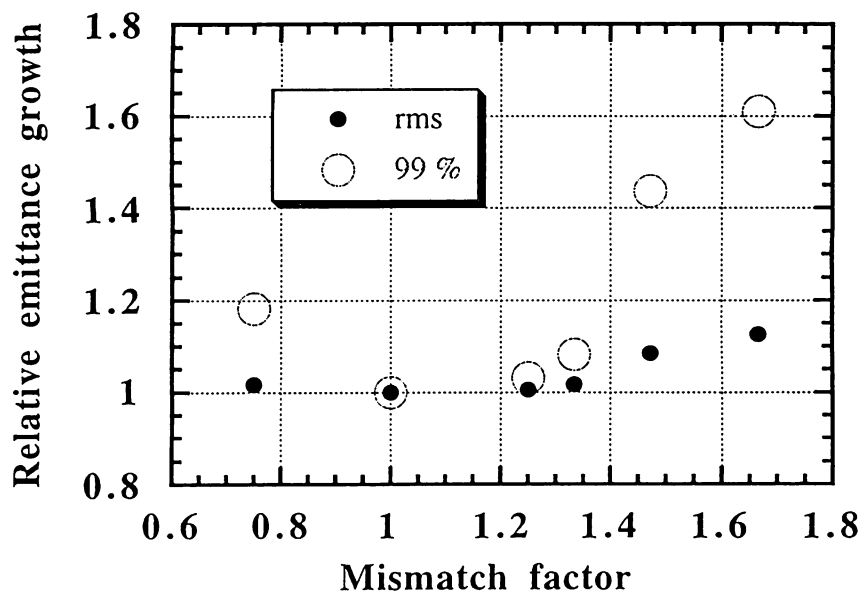


Fig. 4.12 Longitudinal emittance growth (rms and 99%) as a function of the mismatching factor at the entrance of the DTL. The growth is normalized by that for the matched injection. The injection beam of type (B) was used. A mismatching factor of 0.96 corresponds to the injection beam from the MEBT.

As for the mismatch in the transverse motion, it is widely known that it causes beam halos in the output beam. Figure 4.13 shows the calculated rms beam sizes in the x-direction for the matched injection beam and the mismatched injection beam. The corresponding output profiles are shown in Figs. 4.14 and 4.15.

In conclusion, the transverse matching should be done exactly by tuning four focusing magnets in the MEBT. As for the longitudinal matching, although the approximately matching can be obtained by using a buncher, we propose two-buncher system in order to achieve matching for increasing in the peak current.

There is another matching section between the DTL and the SDTL, named high-energy beam-transport line (HEBT). Four quadrupole magnets, including the last two magnets in the drift tube, should be used for the transverse matching. Figure 4.16 shows the relative longitudinal emittance growth in the SDTL as a function of one of the twiss parameters ( $\beta$ ) at the entrance of the SDTL. It seems that the dependence of both rms and 99% emittances upon the matching at the entrance is not so large, suggesting that a longitudinal matching device is not necessary. However, a buncher may be useful for varying the energy width of the output beam. This point should be further studied in connection with the debuncher operation.

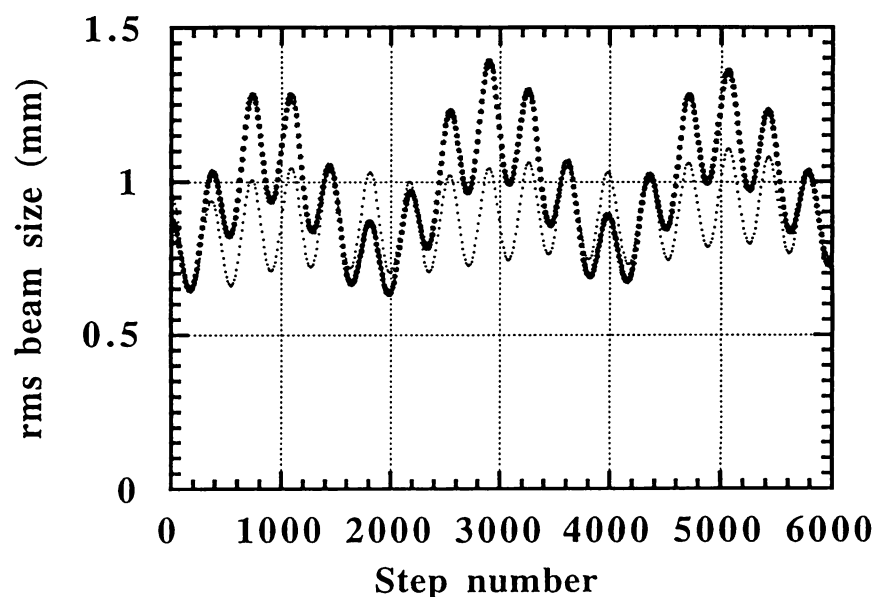


Fig. 4.13 Variation of the rms beam size in the x-direction for the matched injection beam (thin curve) and the mismatched injection beam (wider curve) during initial 33 cells in acceleration from 3 MeV in the DTL. A mismatch factor is about 0.85.

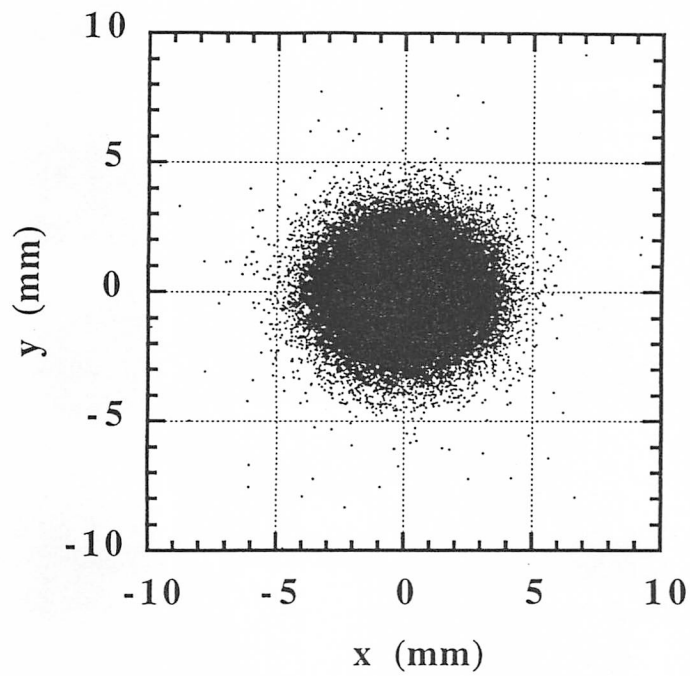


Fig. 4.14 The output profile of the matched injection simulation. The number of particle is 48000. The corresponding beam-size variation is shown in Fig. 4.13.  $\alpha=0$ .

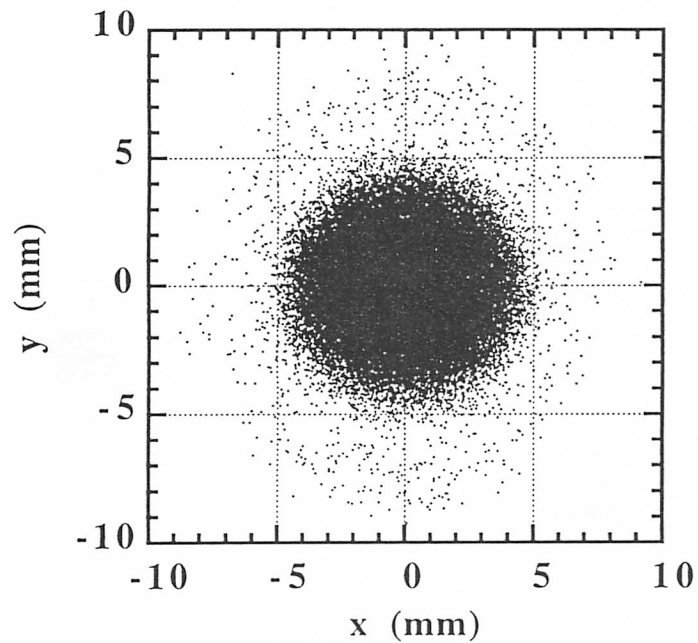


Fig. 4.15 The output profile of the mismatched injection simulation. The number of particle is 48000. The corresponding beam-size variation is shown in Fig. 4.13.  $\alpha=0$ .

### 4.3.7 ZTT optimization

From the viewpoint of total accelerator efficiency, a choice of rf structures for the medium energy is very important, since the effective shunt impedance (ZTT) of DTL decreases rapidly as the energy increases and that of a coupled cavity linac (CCL) usually decreases rapidly as the energy decreases. The separated-type drift tube linac (SDTL) is one of the most promising candidate for the medium-energy accelerator structure. The higher ZTT for SDTL is expected since the optimization of cavity geometry can be freely performed without any restriction from size of the electro-quadrupole magnet in the drift tubes. Figure 4.17 shows the effective shunt impedances for DTL, SDTL and the annular coupled structure (ACS). Comparison of main parameters for DTL and SDTL are summarized in Table 4.7. In conclusion, a complex of DTL and SDTL up to an energy of 200 MeV shows the highest performance [1] among many number of various type of linac complexes. In addition, it can be achieved by using one operating frequency, which brings many advantages not only in beam-dynamics issues but also in both construction and operating ones.

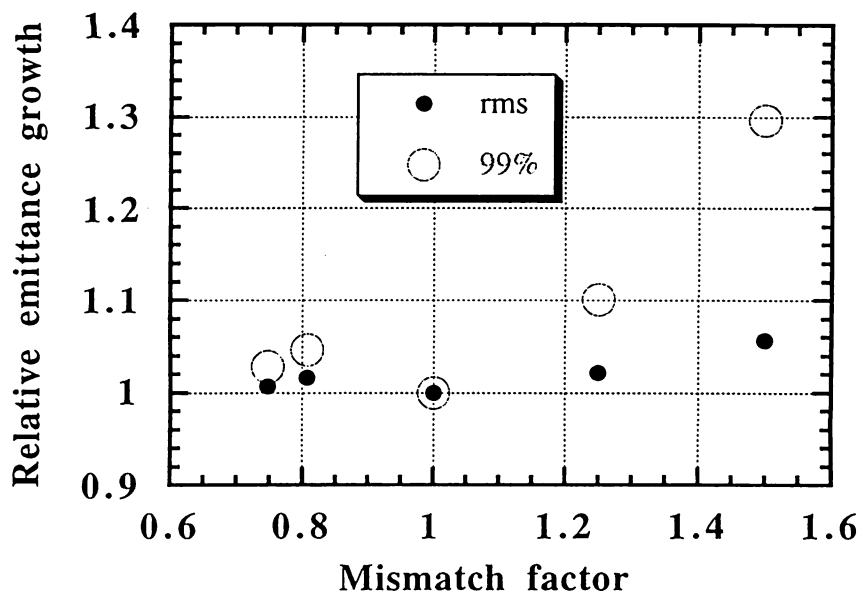


Fig. 4.16 Relative longitudinal emittance growth in the SDTL as a function of mismatch factor at the entrance of the SDTL. The growth is normalized by that with the matched condition calculated with Trace-3D code. A mismatch factor of about 0.81 corresponds to the direct injection of the DTL output beam into the SDTL.

Table 4.7 Typical parameters of the DTL and SDTL structures at a frequency of 324 MHz and an energy of 50 MeV ( $\beta=0.31$ ).

	DTL	SDTL	
Tank diameter	56	52	cm
DT diameter	13	9	cm
Bore radius	1.3	1.5	cm
Outer corner radius	2.5	2.2	cm
Inner corner radius	1.0	0.5	cm
Z	78.2	75.9	M $\Omega$ /m
T	0.703	0.830	
ZTT	38.6	52.3	M $\Omega$ /m
Esurface peak	4.02	5.87	MV/m

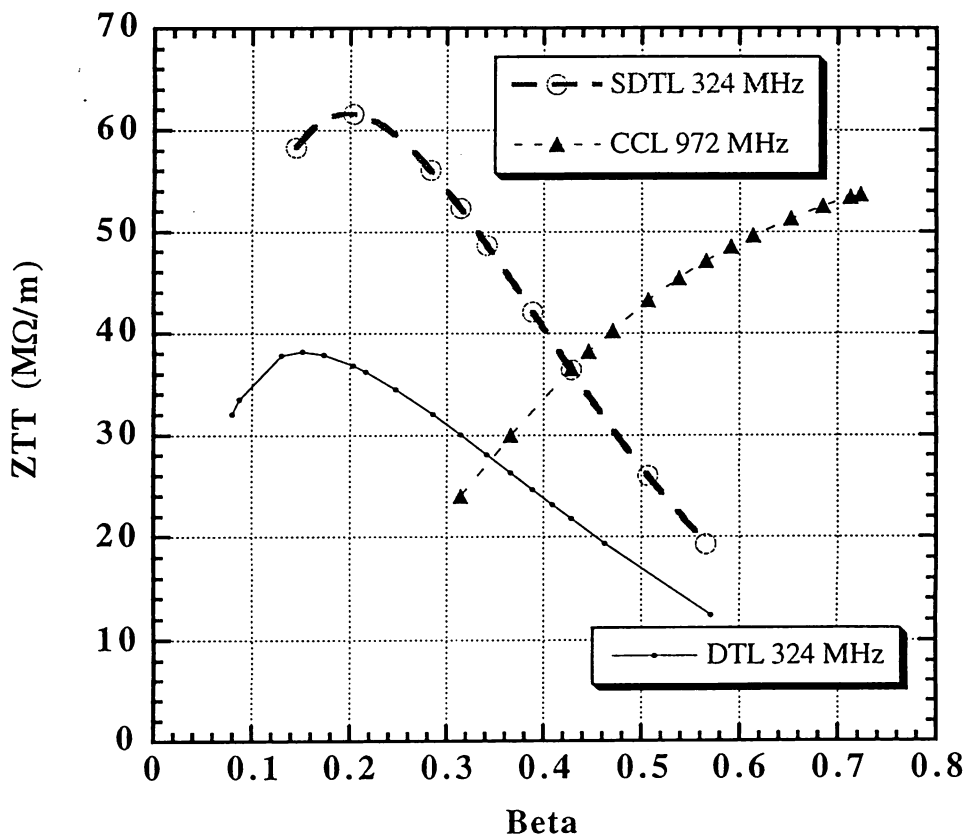


Fig. 4.17 Effective shunt impedances used for the JHF proton linac.

### 4.3.8 Emittance growth and beam halos

The emittance growth during acceleration is related to any energies associated with accelerated particles such as kinetic energies, potential energies due to external focusing forces, field energies within a bunch and mismatched energies [15]. The other sources of the emittance growth is non-linear effects associated with acceleration such as non-linearity of rf fields, transverse focusing forces and non-linear space-charge forces including collision effects.

Some preliminary results for emittance growth and halo formation have been obtained by using code LINSAC [14]. In the code, it is possible to control the effects of collision in a bunch by modifying parameters ( $\alpha$ ) for a Coulomb potential: a simulation with  $\alpha=0$  means that with the space-charge effects including the collision effects, and one with  $\alpha=1$  means that with the space-charge effects but without the collision effects. It is known that most linac simulation codes in the world take account of the space-charge effects as an average force derived from the electric potential and do not take account of the collision effects. Here, the results of simulations with the collision effects are presented. Since there are some overestimates of the collision effects in the macro-particle simulations, careful analyses of the simulation results are required.

Some simulations from 3 to 148 MeV in a 324-MHz drift tube linac for two kinds of focusing methods (equipartitioning focusing method and constant phase advance focusing method) and two kinds of  $\alpha$  ( $\alpha=0$  and  $\alpha=1$ ) were performed. Variations of the rms emittances along the linac are presented in Fig.4.18. Normalized rms transverse ( $\epsilon_{x\text{rms}}$ ) and longitudinal ( $\epsilon_{z\text{rms}}$ ) emittances of  $0.19 \pi\text{mm}\cdot\text{mrad}$  and  $0.36 \mu\text{m}$  ( $0.13 \pi\text{MeV}\cdot\text{deg}$ ) were used for a 30-mA injection beam. The longitudinal emittances of the output beam for both focusing methods are plotted in Fig. 4.19. The results show the following features:

- 1) The amount of rms emittance growth depends upon the type of focusing method.
- 2) The longitudinal emittance growth in the constant phase focusing is much larger, in comparison with that in the equipartitioning focusing. On the contrary, the transverse emittance growth in the equipartitioning focusing, in which the transverse phase advance in the high-energy region becomes small, is a little larger than that in the constant phase focusing.
- 3) The effects of the free parameter ( $\alpha$ ) on the longitudinal emittance growth in the equipartitioning focusing is very small, while they are very large in the constant phase focusing.

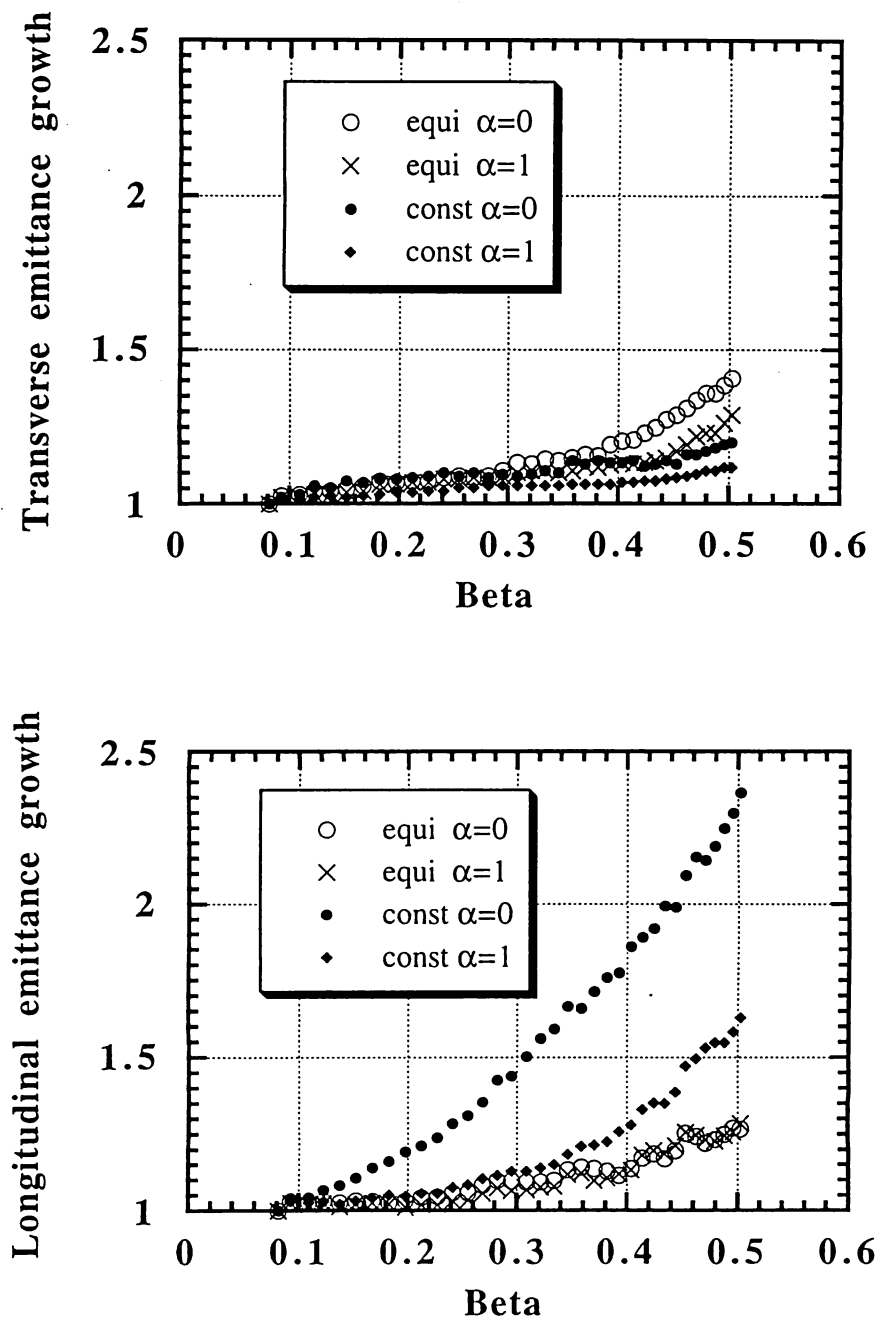


Fig. 4.18 Variation of rms-emittance growth factors during acceleration for the simulations with the equipartitioning focusing method and the constant phase advance method. The results for  $\alpha=0$  and  $\alpha=1$  simulations are presented. The number of particles is 3200.

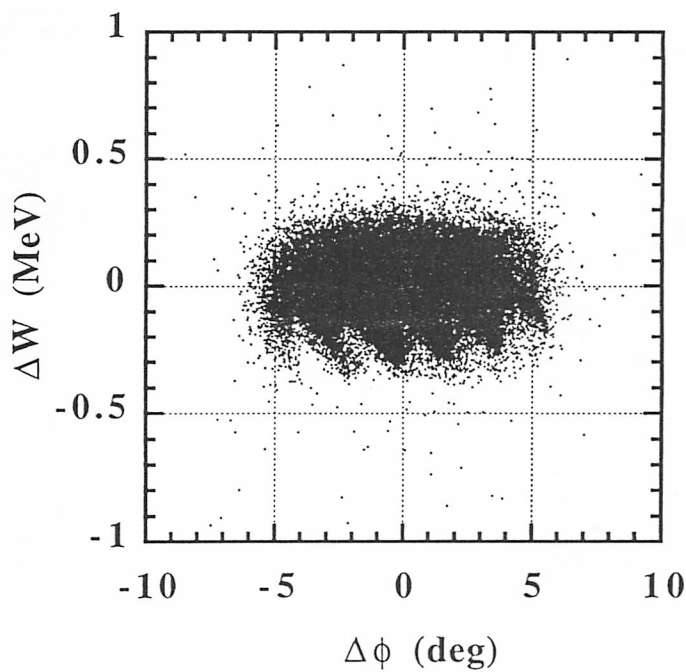
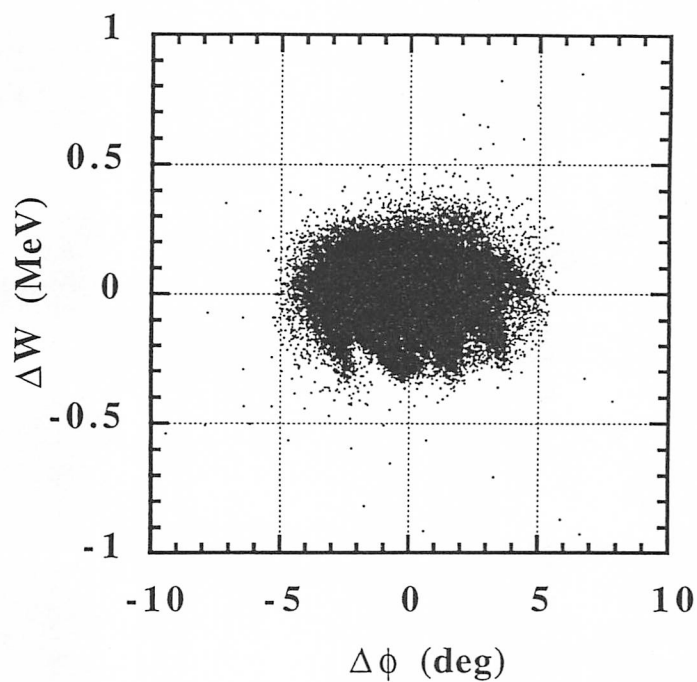


Fig. 4.19 Longitudinal emittances after acceleration from 3 to 148 MeV. The upper is results with the equipartitioning focusing method. The lower is results with the constant phase advance method. The number of particles is 48000. The beam current is 30 mA.  $\alpha=0$ .

- 4) The effects of the free parameter ( $\alpha$ ) on the transverse emittance growth can be seen in the both focusing methods; they are rather small compared with that on the longitudinal emittance growth in the constant phase focusing.
- 5) A mismatched injection in transverse phase space causes a number of halo-like particles in the output profile.
- 6) The effects of the free parameter ( $\alpha$ ) in producing halo-like particle can be observed. It is noted that the number of halo-like particles in the longitudinal phase space for the constant phase simulation is relatively large.

In the equipartitioning focusing method with a equipartitioned injection beam, there is not large longitudinal emittance growth, resulting in nearly the same amount of the emittance growth for both phase spaces.

Regarding beam losses, a beam-halo problem has become a matter of great concern, and a summary of the mechanism of producing of beam halos has been reported [16]. The beam-halo problem has three aspects. The first is an intrinsic mechanisms concerning the formation of beam halos. The second is related to selecting the accelerating parameters. The third involves some possible errors in accelerating the beam, which cause additional degradation of the beam properties. Strictly speaking, they are not independent, since selecting and tuning the accelerating parameters determine the greatest part of the macroscopic beam properties, which in turn influence the effects of halo formation. Preliminary results of ratio of beam halos calculated with the code LINSAC are summarized in Table 4.8. Here, halo-like particles are defined by those in the outside of 6.5 times the standard deviation of the radial distribution of the output beam. It can be concluded that the simulation with 48000 particles shows the ratio of halo-particle of order of  $10^{-4} \sim 10^{-3}$ . In connection with the matching of the beam at the injection point in the matched simulation, it can be said that there are almost no halo-like particles in the matched simulation with  $\alpha=1$ , while there are some halo-like particles in the matched simulation with  $\alpha=0$  (Fig. 4.14). This suggests that the main reason for production of the halo-like particles in the matched simulation is not the inadequacy of matching in the injection of the beam but the collision effects. In order to discuss beam halos of less than the order of  $10^{-4}$  qualitatively and accurately, a simulation with the macro particle number of more than 48000 is desirable.

Table 4.9 shows the summary of halo-like particles in the longitudinal motion. Here, halo-like

---

Table 4.8 Ratio of halo-like particles in the output beam profile calculated with the LINSAC simulation. The number of particles is 48000.

type of simulation	focusing type	$\alpha$	rate of halo-like particles in %
(1) matched-macro	equipartitioning	0	0.1 (Fig. 4.14)
(2) mismatched-macro	equipartitioning	0	0.7 (Fig. 4.15)
(3) matched-macro	equipartitioning	1	0
(4) matched-real	equipartitioning	0	0.05
(5) matched-real	equipartitioning	1	0
(6) mismatched-macro	equipartitioning	0	0.085 (25% error in $\beta_x$ )
(7) mismatched-macro	equipartitioning	1	0.02 (25% error in $\beta_x$ )
(8) matched-macro	constant phase	0	0.08

note:

1. “macro” simulation means a simulation using a macro particle with macro charge much larger than a unit charge.  
“real” simulation means a simulation using a unit-charged particle instead of a macro-charged particle.
2. In the simulations (6) and (7), one of the twiss parameter at the injection point ( $\beta_x$ ) is increased by 25% from that for the matched injection.
3.  $\alpha=1$  means that the simulation does not take account of the collision effects.

Table 4.9 Ratio of halo-like particles in the output longitudinal emittance calculated with the LINSAC simulation. The number of particles is 48000.

type of simulation	focusing type	$\alpha$	rate of halo-like particles in %
(1) matched-macro	equipartitioning	0	0.098 (Fig. 4.19 upper)
(2) matched-macro	equipartitioning	1	0.03
(3) matched-macro	constant phase	0	0.19 (Fig. 4.19 lower)
(4) mismatched-macro	equipartitioning	0	0.32 (+25% error in $\beta_z$ )
(5) mismatched-macro	equipartitioning	0	0.11 (-25% error in $\beta_z$ )

note:

1. In the simulations (4) and (5), one of the twiss parameter at the injection point ( $\beta_z$ ) is increased by  $\pm 25\%$  from that for the matched injection.

particles are defined by those in the outside of 12.5 times the longitudinal output rms emittance. It can be seen that the number of halo-like particles in the constant phase simulation is approximately twice as large as that in the equipartitioning simulation. It can also be seen that the mismatch injection in the longitudinal phase space causes additional increase in the halo-like particles, especially in the case of wider phase spread ( $+25\% \beta_z$ ).

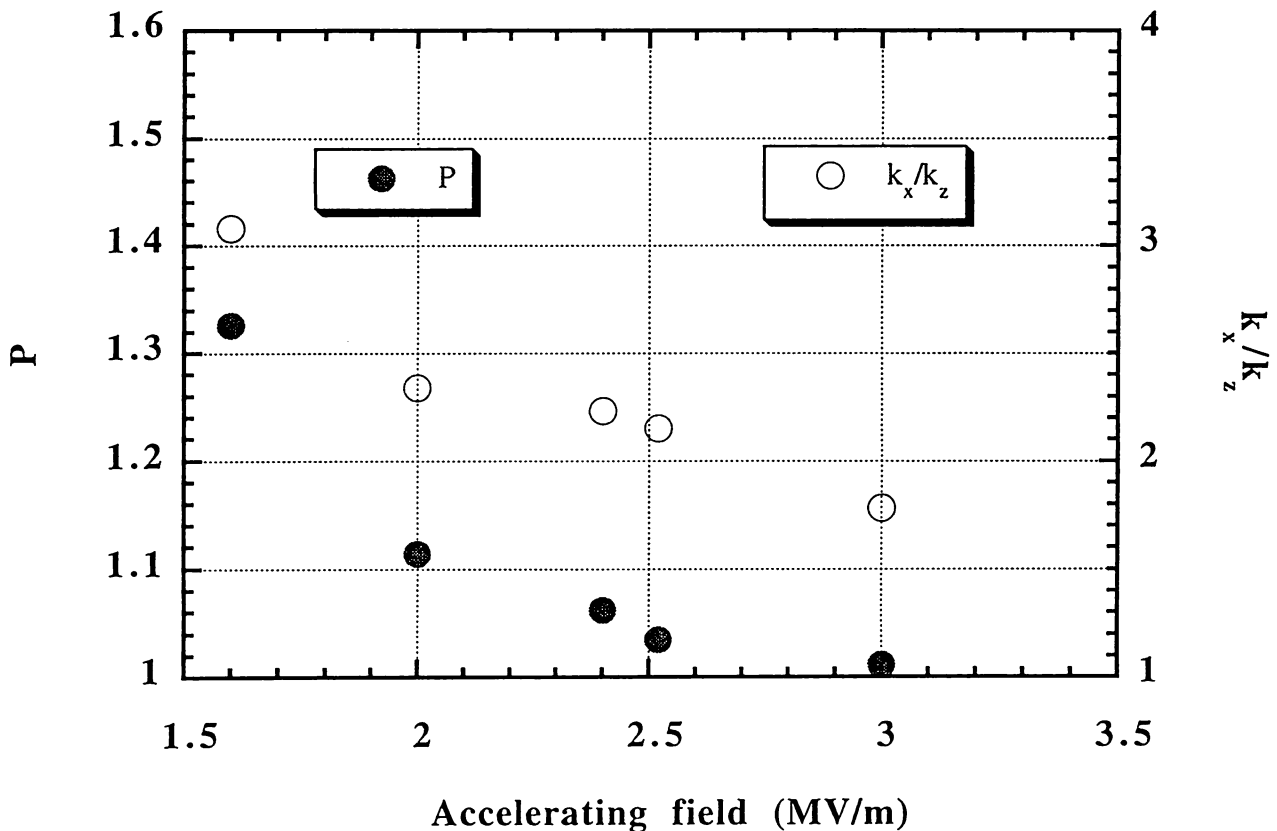


Fig. 4.20 Equipartitioning parameters and ratio between transverse focusing force and longitudinal one as a function of an accelerating field at a 3-MeV injection point.  $5x\epsilon_{x,rms}=1.5 \pi \text{mm-mrad}$  and  $5x\epsilon_{z,rms}=2.6 - 2.9 \times 10^{-6} \text{ m}$  are assumed.  $P$  is defined by  $\epsilon_{nx} z_m / e_{nz}$ .  $k_x$  and  $k_z$  are the wave numbers, including space-charge effects, for transverse and longitudinal phase oscillations, respectively. The beam current is 30 mA.

### 4.3.9 The drift tube linac (DTL)

The DTL accelerates the beam from 3 to 50 MeV with three tanks. Details of the parameters are summarized in Table 4.14 in section 4.3.15. Each tank is stabilized with post couplers [17] in order to suppress the effects of perturbations due to both beam loadings and fabricating errors. The maximum electric field on the surface of drift tubes is less than the Kilpatrick field limit (17.8 MV/m), suggesting that there is almost no discharge problem during operation.

An accelerating field of 2.5 MV/m for the first tank is chosen by following reasons:

1. A sufficiently large longitudinal focusing strength at the injection part is desirable. Figure 4.20 shows equipartitioning parameter ( $P$ ) and ratio between transverse focusing force and longitudinal one as a function of an accelerating field at a 3-MeV injection point. If an accelerating field of 1.6 MV/m is selected, the ratio of transverse and longitudinal focusing strength becomes more than three. Preliminary results of simulation with constant transverse phase advance focusing method indicate that a ramped field gradient from 1.6 to 2.4 MV/m in the first DTL tank causes an additional increase in the rms longitudinal emittance of 6% compared

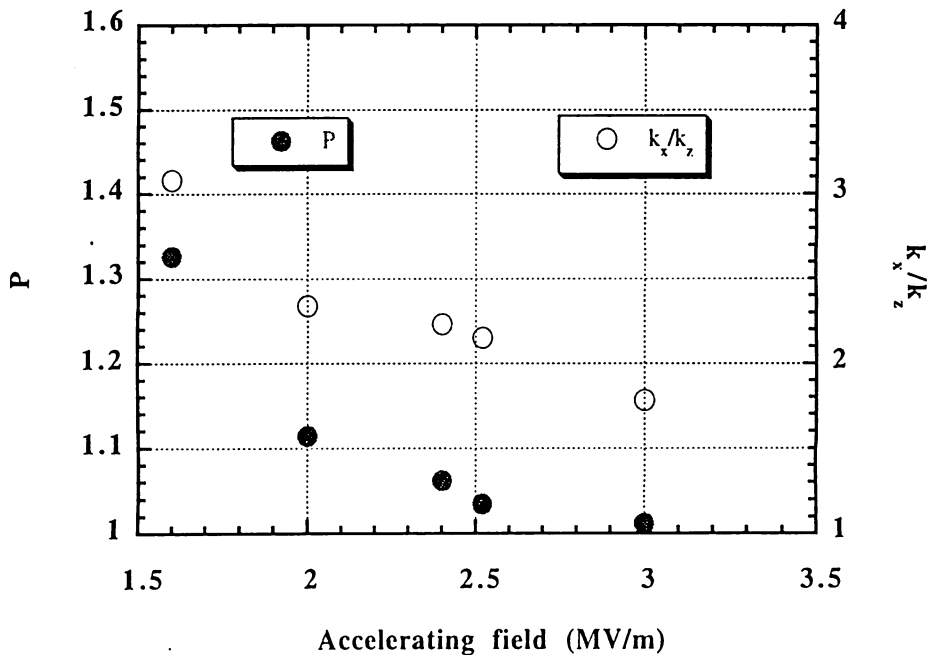


Fig. 4.20 Equipartitioning parameters and ratio between transverse focusing force and longitudinal one as a function of an accelerating field at a 3-MeV injection point.  $5x\epsilon_{x,rms}=1.5 \pi\text{mm}\cdot\text{mrad}$  and  $5x\epsilon_{z,rms}=2.6 - 2.9 \times 10^{-6} \text{ m}$  are assumed.  $P$  is defined by  $\epsilon_{nx} z_{nt}/e_{nz} a$ .  $k_x$  and  $k_z$  are the wave numbers, including space-charge effects, for transverse and longitudinal phase oscillations, respectively. The beam current is 30 mA.

with that with constant field gradient of 2.4 MV/m.

2. Equipartitioned beam injection is desirable if possible. It is seen from Fig. 4.20 that a higher accelerating field is desirable from the viewpoint of equipartitioned input beam. However, more careful studies are required since this depends largely upon the beam properties from the RFQ.
3. A high accelerating field, which might cause discharge problem in the tank, is not desirable.
4. A high rf power efficiency, including both rf excitation and beam loading, is desirable.
5. A nearly matched longitudinal injection can be achieved.

The coupled envelope equations and the equipartitioning theory are used for the focusing design [11-13]. The typical focusing parameters along the linac are shown in Fig. 4.8 in section 4.3.5. The

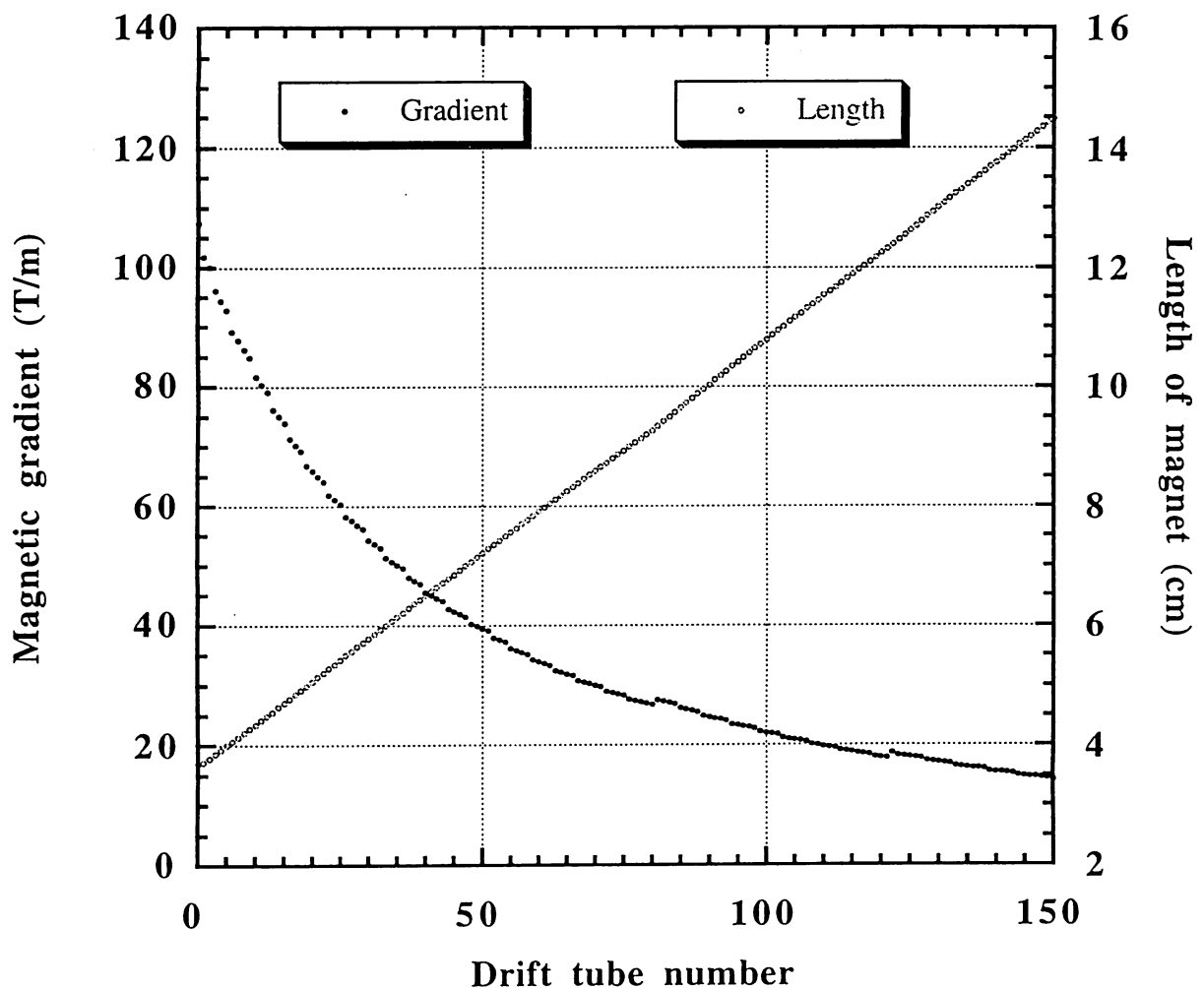


Fig. 4.21 The required magnetic field gradient and the length of magnets in the DTL.

required magnetic field gradient and the length of the magnet are plotted in Fig. 4.21. Since the transverse beam size increases gradually along the linac, a ratio of transverse to longitudinal beam size gets close to unity as acceleration. Therefore, a bore radius of the drift tube for each tank varies by three steps; 6.5, 11 and 13 mm. The results of beam simulation are presented in the next section together with those in the SDTL.

### 4.3.10 The separated-type drift tube linac (SDTL)

The SDTL [3] accelerates the beam from 50 to 200 MeV. The typical configuration is shown in Fig. 4.22. The SDTL has several merits as follows:

1. it contributes to obtain the better beam qualities by separating the transition point in the transverse motion from that of the longitudinal motion, compared with a CCL scheme with a relatively lower transition energy and a frequency-multiply factor of three [1],
2. a higher effective shunt impedance can be achieved for the total accelerating system,
3. the fabrication and alignment of the drift tubes and tanks become easier compared with that of a conventional DTL, resulting in a reduction in the construction cost as well as a reduction in the number of focusing magnets, and
4. since a unit tank of the SDTL consists of several numbers of unit cells, stabilizing devices are not necessary, resulting in a more simple structure compared with the DTL.

It also has demerits as follows:

1. the number of unit tanks increases,
2. the number of drift spaces between two adjacent unit tanks increases, and
3. the number of tuning parameters increases.

The results of the beam simulation shows that the degradation of the longitudinal beam quality due to the additional drift spaces mentioned above is about 10%. It is negligibly small.

There are several features in designing as follows:

1. Number of unit cells in a tank holds constant in order to avoid an abrupt change in the transverse focusing period.

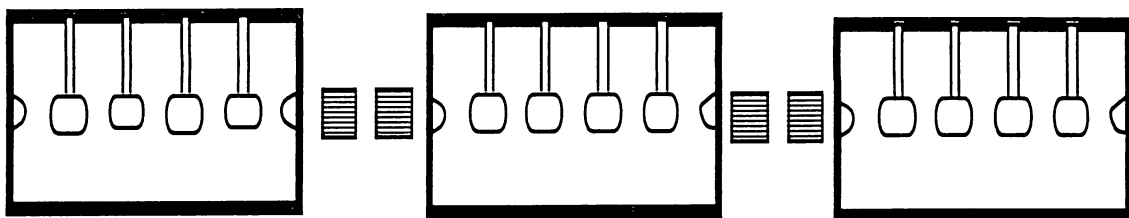


Fig. 4.22 Schematic view of the SDTL structure. The focusing magnets are indicated by squares.

2. A doublet focusing scheme is adopted in order to obtain sufficiently large acceptance.
3. Equipartitioning focusing method is adopted, which allows smooth connection of focusing parameters to those in DTL part.
4. A rather high average accelerating field is chosen for the limited total length of the linac. The peak surface electric field is as large as 1.3 times the Kilpatrick field limit.

Figure 4.23 shows variation of the rms beam sizes for three directions along the linac. Some longitudinal mismatching can be seen after injection into the SDTL (after step number of 27150) since the output beam of the DTL was injected with only a transverse matching. Since the transverse beam sizes becomes large as the energy increases, the bore radii of the drift tubes also increase in order to achieve sufficiently large safety factor (Fig. 4.24). Figure 4.25 shows the calculated emittance growth (rms and 99%) with a 30-mA injection beam of type-B in acceleration from 3 to 200 MeV.

Judging from the simulation results by LINSAC, the focusing strength is closely related to the output beam qualities in the linac. The calculated emittance growth with a 60-mA type-B injection beam is shown in Fig. 4.26. Here, two kinds of the focusing strength in the SDTL were examined (Fig. 4.27): one (SDTL-1 in Fig. 4.27) is the optimized focusing parameters for a 30-mA beam and

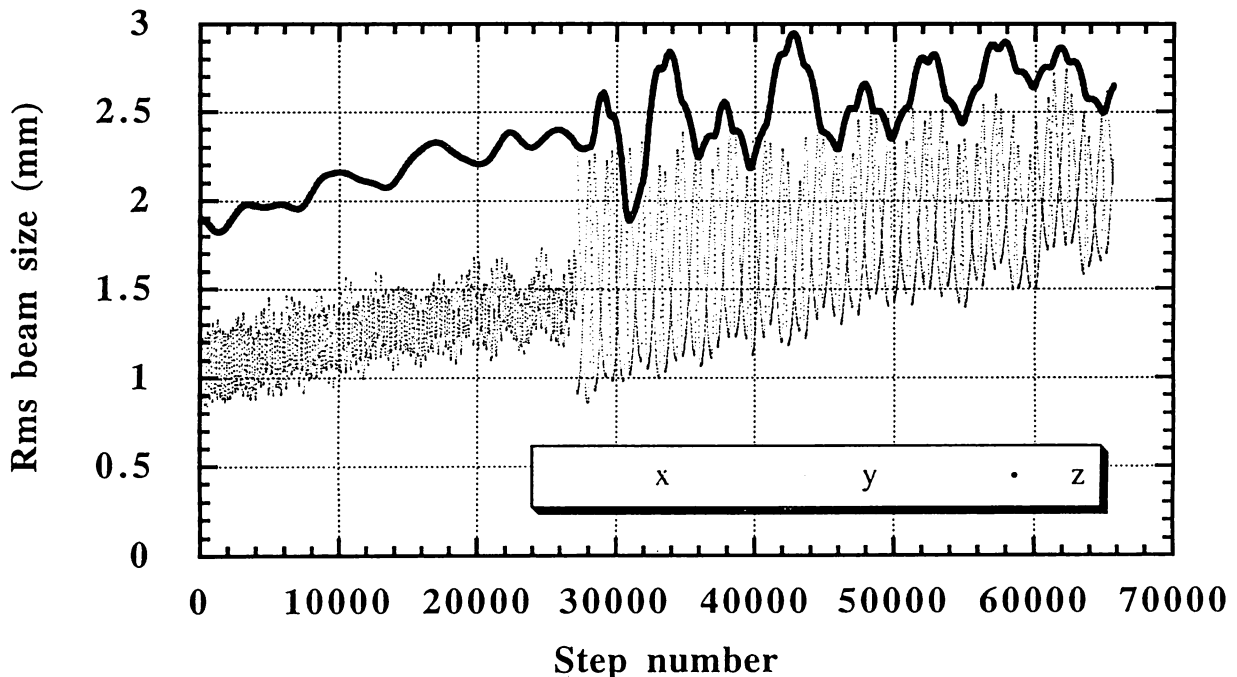


Fig. 4.23 Calculated rms beam sizes along the linac. A unit cell corresponds to 181 steps. The injection particles of type-B in Table 5 are used.  $\alpha=0$ .

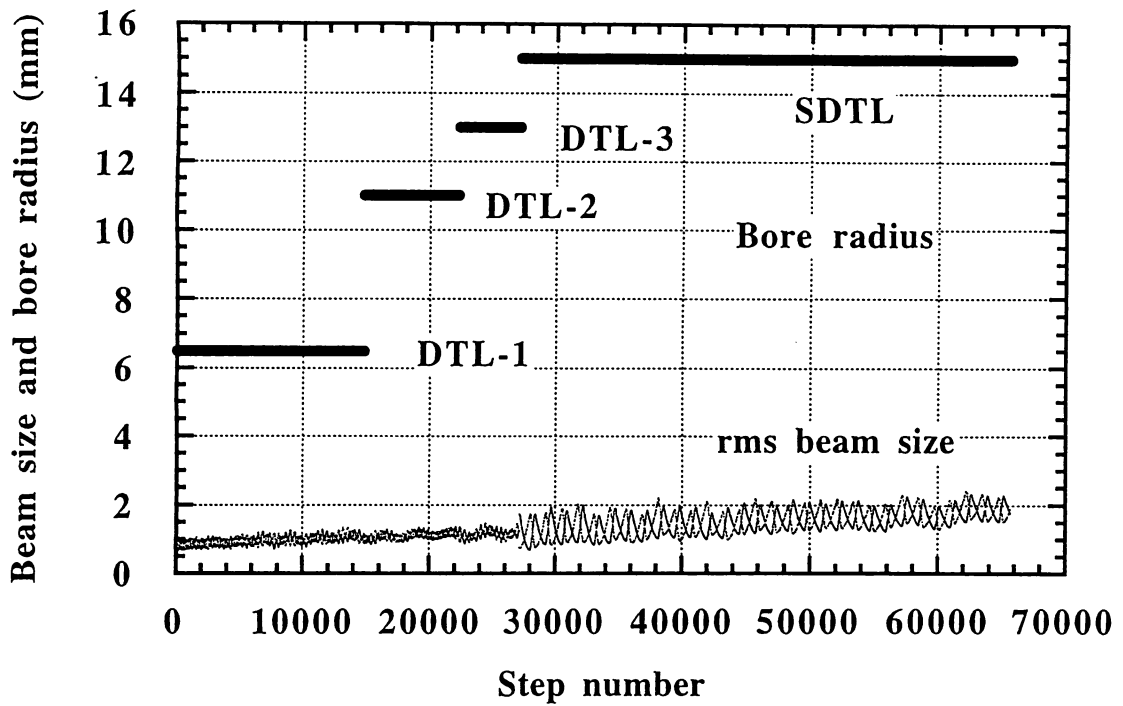


Fig. 4.24 Variation of rms transverse beam size and bore radii along the linac. One cell corresponds to 181 steps.  $\alpha=0$ .

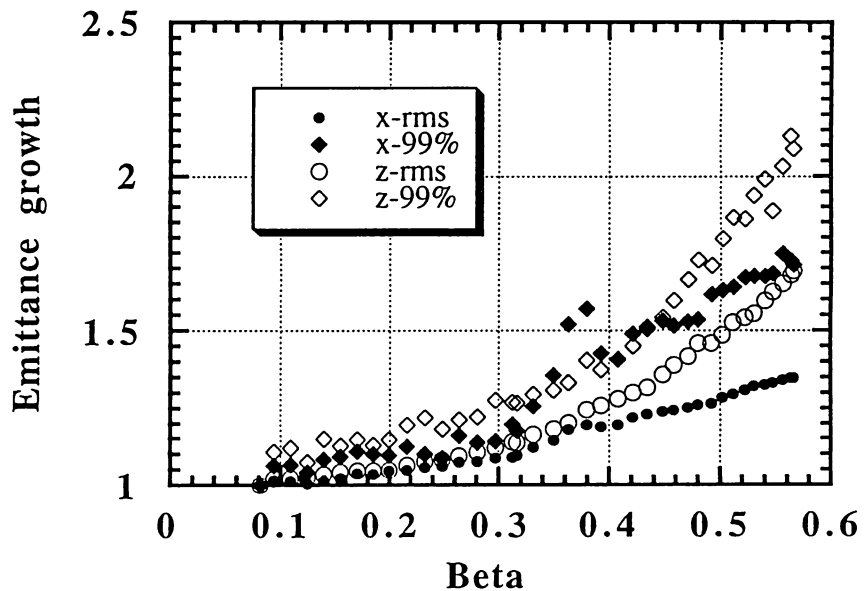


Fig. 4.25 Transverse emittance growth (rms and 99%) along the linac. A 30-mA type-B injection beam is used.  $\alpha=0$ .

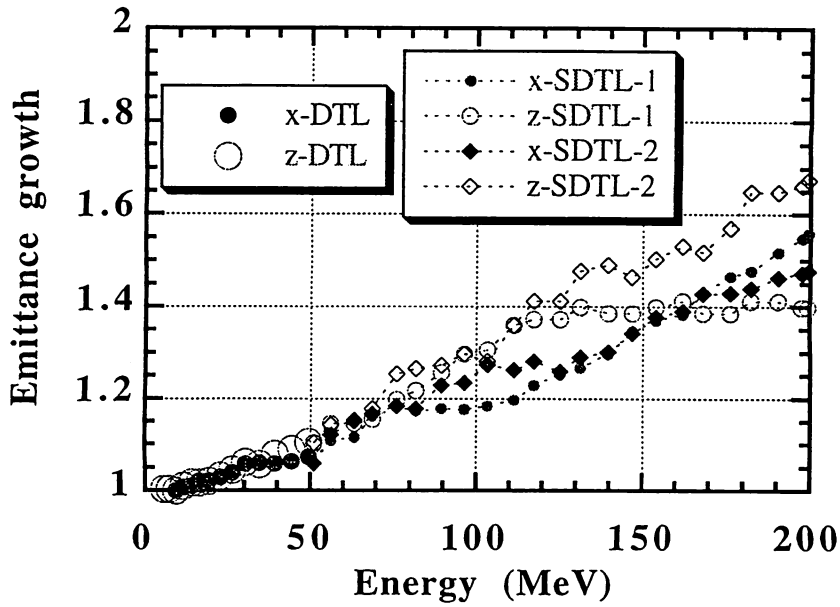


Fig. 4.26 Calculated rms emittance growth with a 60-mA type-B injection beam in acceleration from 3 to 200 MeV. The results for two kinds of the focusing strength in the SDTL (shown in Fig. 24) are plotted.  $\alpha=0$ .

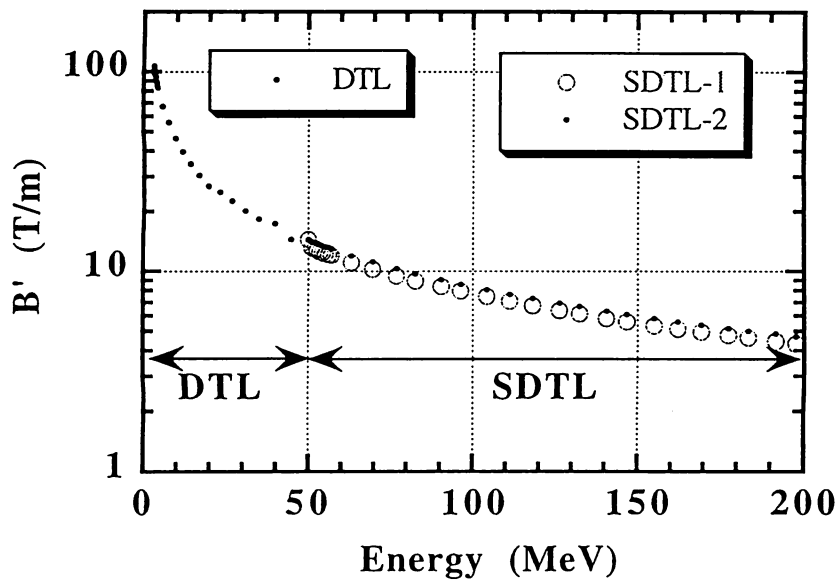


Fig. 4.27 Variation of the focusing strength along the linac. Two kinds of focusing strength in the SDTL were plotted: one (SDTL-1) is the optimized focusing parameters for a 30-mA beam and another (SDTL-2) is those for a 60-mA beam. The difference between them is about 8%.

another (SDTL-2 in Fig.4.27) is those for a 60-mA beam. The latter is stronger by about 8% than the former. There are some differences in transverse and longitudinal emittance growth ratios due to the focusing strength. Therefore in the practical operation, the transverse focusing can be tuned in order find optimum emittance growth in both transverse and longitudinal phase spaces.

The effects of errors in rf fields in the SDTL acceleration were extensively investigated and reported in Section 3.7.4 of ref. [1]. The results obtained there were as follows:

- 1) the longitudinal emittances as well as the energy spread increases as the field errors,
- 2) the beam loss increases as the field errors, which gives tolerances for the field errors,
- 3) the transverse emittances do not change much.

If we set the limit of the beam loss below 0.1 - 0.2%, the allowable amplitude error for each cell is  $\pm 1\%$ , for each tank  $\pm 3\%$  and the phase error for each tank  $\pm 4\%$ . The phase errors for each cell within a unit tank can be set zero for the SDTL structure.

### 4.3.11 The coupled cavity linac (CCL)

Preliminary beam-dynamics calculation regarding the first-stage linac structure of an output energy of 200 MeV and upgrade of an output energy from 200 to 400 MeV by using CCL-type structure is reported in ref. [1]. There, a number of simulations with different types accelerator complex were performed. Then, it was concluded that an accelerator complex of DTL, SDL and the annular coupled structure (ACS) is a good choice from the viewpoints of both the output beam quality and the accelerating efficiency. There, a frequency of 972 MHz, three times the fundamental frequency, and a transition energies of above 150 or 200 MeV is selected.

### 4.3.12 Debuncher

The required momentum spread of the injected beam into the ring is  $\Delta p/p = \pm 0.1\%$  (full width), and thus a full energy spread of  $\pm 0.365$  and  $\pm 0.680$  MeV for the output energies of 200 and 400 MeV, respectively. In order to satisfy the requirement above mentioned, debunching systems placed in the beam-transport line between the linac and the ring is necessary. A preliminary beam-transport line, consisting of both a matching section with four quadrupole magnets and a number of FODO section, was used for a multi-particle simulation by using the code LEBT [10]. Since the purpose of the simulation was to estimate the longitudinal behavior along the transport-beam line, the motion in the transverse phase spaces was not finely tuned against the space-charge effects. The injection particles were delivered from either an SDTL simulation (200 MeV, 324 MHz) or a CCL simulation (400 MeV, 972 MHz). The type-A injection beam was used in the linac simulation. Some errors in an accelerating field in the linac were assumed in order to obtain more realistic spreads of energy and phase in the output beam. Here, random errors of  $\pm 2\%$  in an accelerating field for each cell and each tank and random errors of  $\pm 3\%$  in an accelerating phase for each tank were assumed in the SDTL simulation. No phase errors for each cell was assumed. In the CCL simulation, random errors of  $\pm 2\%$  in an accelerating field both for each cell and each tank, those of  $\pm 1\%$  in an accelerating phase for each cell and  $\pm 3\%$  for each tank were assumed. No errors was assumed in the 50-MeV DTL simulation.

#### A) A debuncher operation for a 200-MeV beam

Variation of rms beam sizes for a 30-mA beam along the beam-transport line is shown in Fig. 4.28. Variation of spreads of phase and energy for a 30-mA beam along the beam-transport line is shown in Fig. 4.29. It can be seen that the energy spread (100% full width) is reduced to 0.271 MeV by means of a debuncher with a voltage of 1.3 MV, located at a distance of 30 m downstream from the linac exit. Figure 4.30 shows the variation of energy spreads along the beam-transport line of 60 m in length for three kinds of debuncher voltage. After passing through a debuncher of 1.3 MV, the energy spread increases along the beam-transport line due to the space-charge effects up to 0.469 MeV at a position of 60 m. The results above mentioned were obtained by collision-less ( $\alpha=1$ ) simulations with 3200 particles. When the number of particles in the simulation increases up to 48000, the energy spread of the SDTL output beam increases by 39%, resulting in a 100% energy spread of 0.506 MeV after the debuncher. The energy spread for four kinds of fraction of the 30-mA, 200-MeV output beam after passing the debuncher of 1.3 MV are listed in Table 4.10. It can be seen from the table that the a beam fraction of 99.9% is within the energy spread of 0.224 MeV for the 48000 particle simulation and that of 0.1% causes an additional energy spread of 0.282 MeV. Therefore, it can be said that a 100% energy spread is only useful if our major concern is a beam loss of order of less than 0.1%. The longitudinal emittances for three positions along the beam-transport line (at the entrance, after the debuncher and at a position of 60 m) for the 48000-particle simulation are shown in Figs. 4.31-4.33. It is seen from Fig.4.33 that an energy spread of

0.575 keV was obtained at a position of 60 m for the 48000 particle simulation. Therefore, it is concluded that the required energy spread can be obtained by using the debuncher for a 30 mA, 200-MeV beam. The transverse rms emittance growth along the beam-transport line is less than 4%.

**B) A debuncher operation for a 400-MeV beam**

**B-1) A peak current of 30 mA**

A similar beam-transport line to that for an energy of 200-MeV was assumed for the 400-MeV beam-transport simulation. Figure 4.34 shows variation of spreads of phase and energy along the beam-transport line. A peak current of 90 mA was used for the beam-transport simulation with 3200 particles, since the CCL frequency of three times the SDTL one was used. A full energy spread of 0.33 MeV was obtained by a debuncher voltage of 1.3 MV, located at a distance of 32 m downstream from the exit of the CCL. It increases up to 0.566 MeV at a position of 60 m. Although the calculated energy width meets the requirement, the phase spread of the beam at the debuncher position becomes very large (~120 degrees), and also the effects of nonlinear rf field become large. Thus, a shorter drift length less than 32 m between the exit of the linac and the debuncher seems to be desirable. In addition, when a peak current from the ion source increases up to more than 60 mA, which means a peak current of 180 mA for the CCL linac with three times the DTL operating frequency, the space-charge effects along the beam-transport line increases largely, resulting in a shorter optimum drift space between the exit of the linac and the debuncher.

**B-2) A peak current of 60 mA**

Figures 4.35 shows the variation of spreads of phase and energy along the 400-MeV beam-transport line of 60 m in length for a 180-mA CCL output beam. A debuncher of 2.1 MV is placed at a distance of 20 m from the entrance of the beam-transport line. It can be seen from Fig. 4.35 that the final energy spread becomes 1.67 MeV at a position of 60 m, which is larger than the requirement. Therefore, another debuncher of 0.6 MV is added at a position of 42.5 m. The calculated results are shown in Fig. 4.36. The final obtained energy spread is 0.774 MeV, which meets the requirement.

Table 4.10 Energy spreads of the 30-mA, 200-MeV output beam after passing the debuncher of 1.3 MV for four kinds of fraction of the beam.

Fraction of the beam	90%	99%	99.9%	100%	
Number of particles in the simulation					
3200	113	177	262	273	keV
48000	104	163	224	506	keV

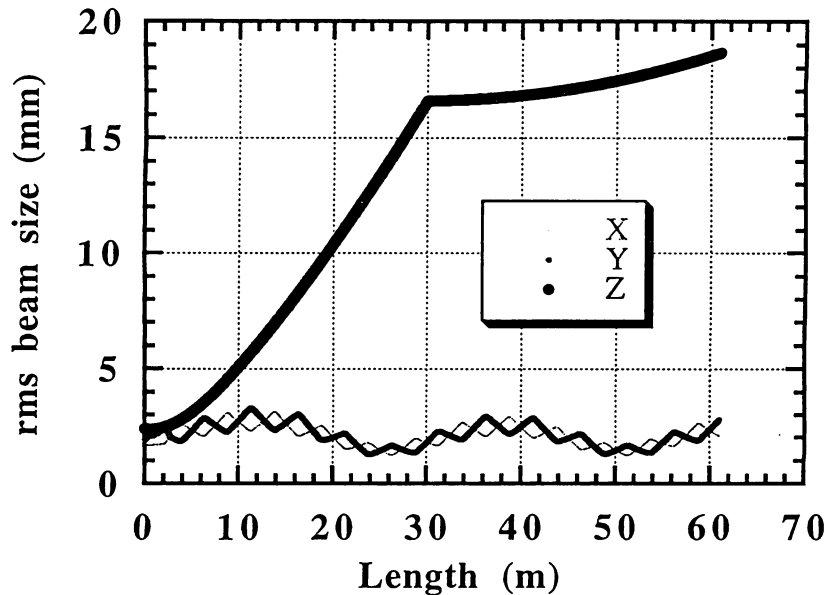


Fig. 4.28 Variation of rms beam sizes along the 200-MeV beam-transport line. A debuncher of 1.3 MV is placed at a position of 30 m from the entrance of the beam-transport line (the exit of the 200-MeV SCTL). The peak current of 30 mA is assumed. The number of particles is 3200.

If the number of particles in the simulation increases from 3200 to 48000, the expected additional increase in the full spread was about 23%, assuming the same ratio for an additional increase in the energy spread as that for the 30 mA, 200-MeV simulation. Then, an expected 100% energy spread becomes 0.952 MeV, which meets the requirement.

### C) Summary

Table 4.11 shows the summarized results of the beam-transport simulation. It is concluded that a momentum spread of  $\pm 0.1\%$  in full width can be achieved for both a 30 mA, 200-MeV beam and a 60 mA, 400-MeV beam.

Table 4.11 Summary of debuncher operation.

Beam	30 mA, 200 MeV	60 mA, 400 MeV	
Debuncher-1 position / voltage	30 m / 1.3 MV	20 m / 2.1 MV	
Debuncher-2 position / voltage	-----	42.5 m / 0.6 MV	
Energy spread(*)	0.469 MeV	0.774 MeV	100% full width

\* Energy spread is one at a position of 60 m from the entrance.

\* Energy spread was calculated with the 3200 particle simulation. An additional increase about 23% was observed when the number of particles in the simulation was 48000.

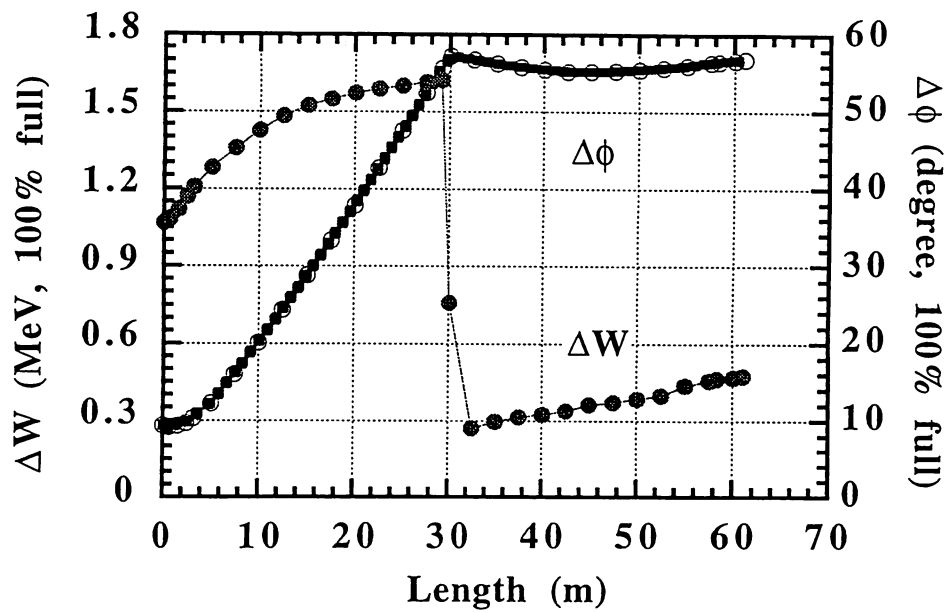


Fig. 4.29 Variation of spreads of phase (in terms of 324 MHz) and energy along the 200-MeV beam-transport line. A debuncher of 1.3 MV is placed at a position of 30 m from the entrance of the beam-transport line. The peak current of 30 mA is assumed. The number of particles is 3200.

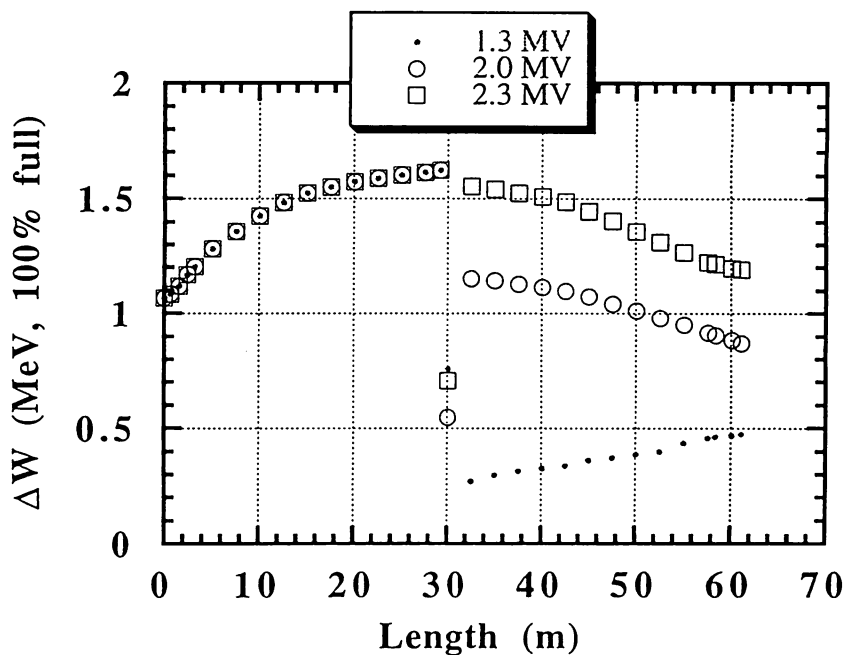


Fig. 4.30 Variation of energy spreads along the 200-MeV beam-transport line. The results for three kinds of debuncher voltage are plotted. A debuncher is placed at a position of 30 m from the entrance of the beam-transport line. The peak current of 30 mA is assumed. The number of particles is 3200.

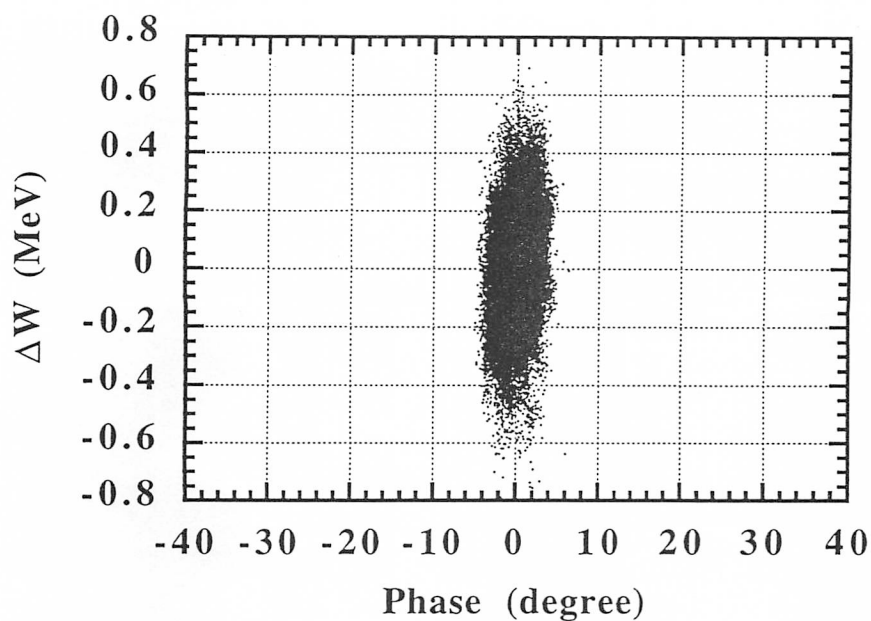


Fig. 4.31 Longitudinal emittance of a 30-mA, 200-MeV beam at the entrance of the beam-transport line (the exit of the 200-MeV SDTL). The number of particles is 48000.

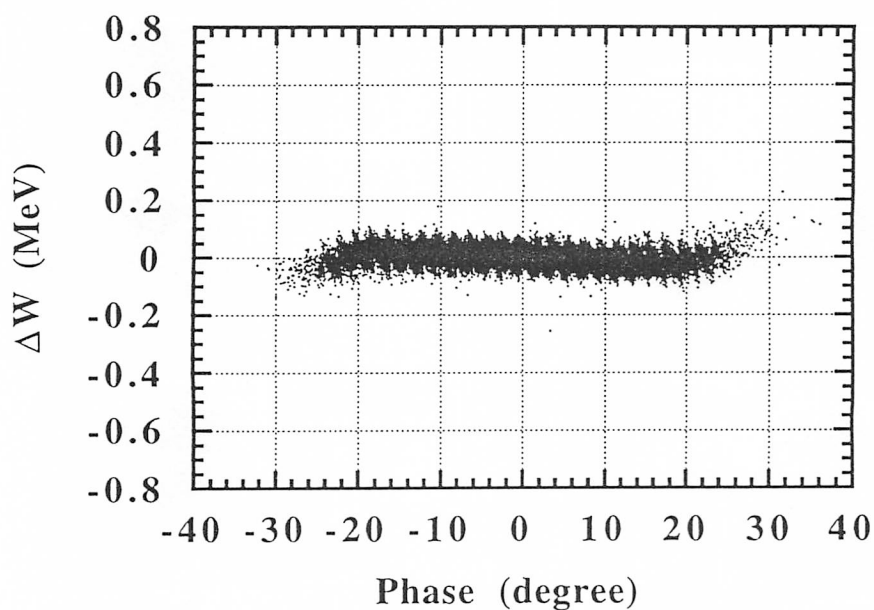


Fig. 4.32 Longitudinal emittance of a 30-mA, 200-MeV beam after the debuncher of 1.3 MV, placed at a position of 30 m from the entrance of the beam-transport line. The number of particles is 48000.

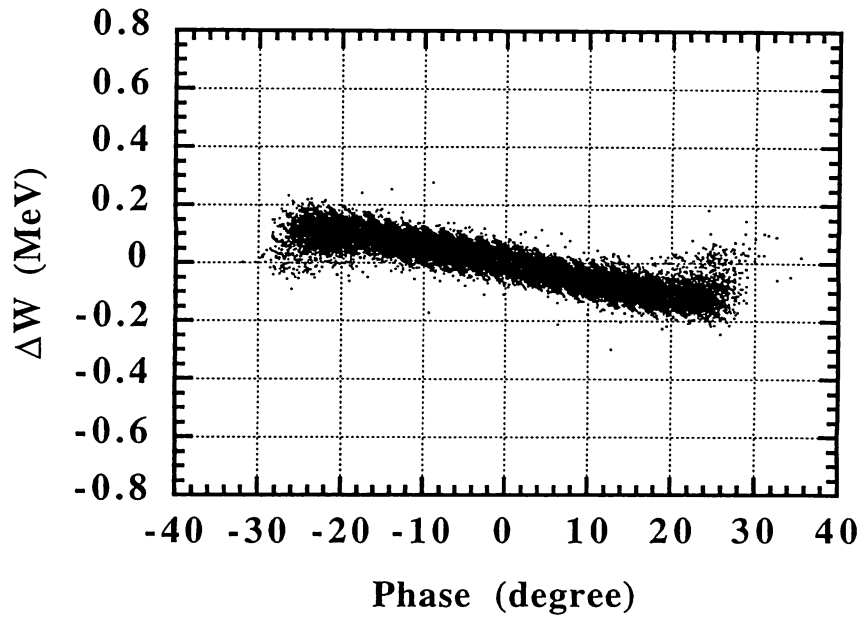


Fig. 4.33 Longitudinal emittance of a 30-mA, 200-MeV beam at a position of 60 m from the entrance of the beam-transport line. The number of particles is 48000.

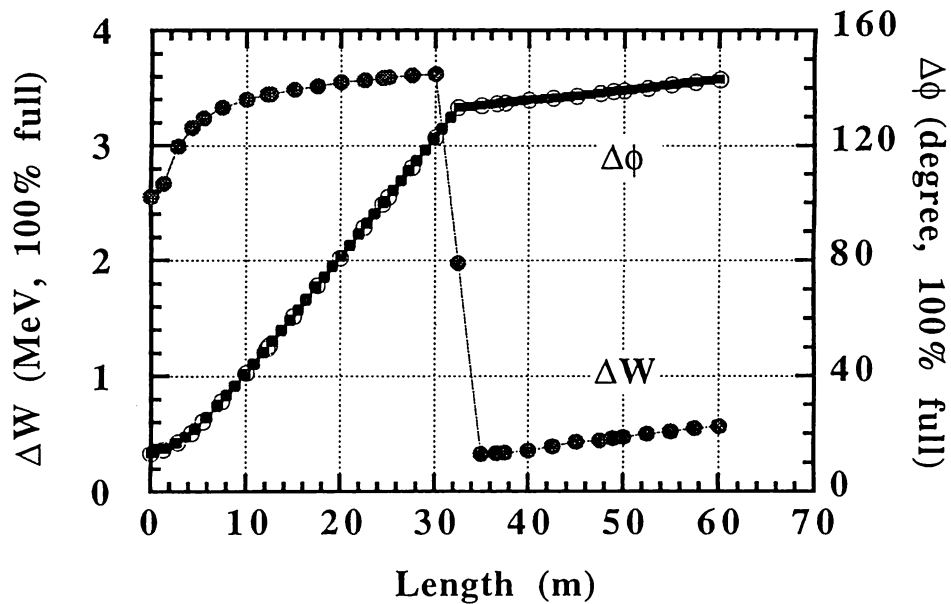


Fig. 4.34 Variation of spreads of phase (in terms of 972 MHz) and energy along the 400-MeV beam-transport line. A debuncher of 1.3 MV is placed at a position of 32 m from the entrance of the beam-transport line. The peak current of 90 mA is assumed. The number of particles is 3200.

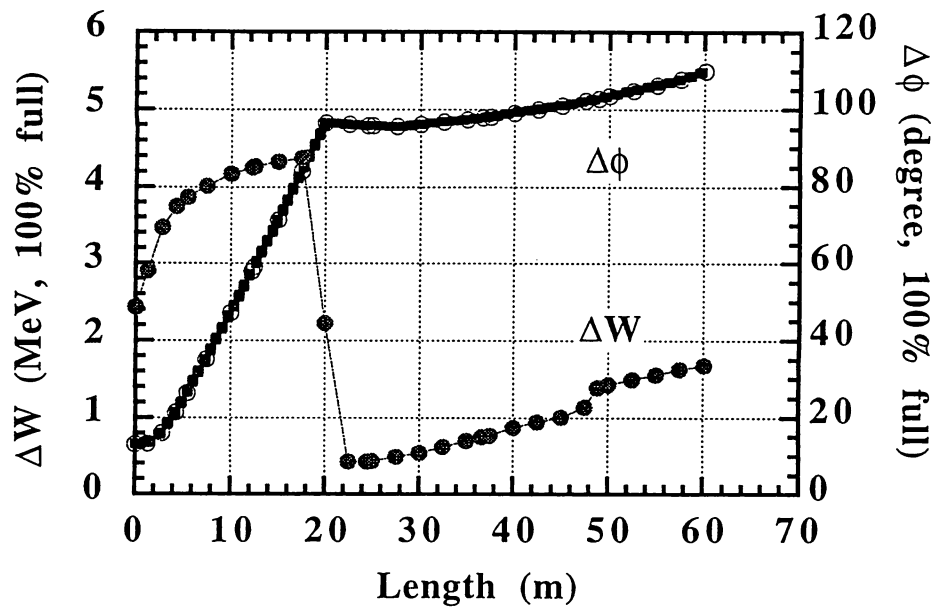


Fig. 4.35 Variation of spreads of phase (in terms of 972 MHz) and energy along the 400-MeV beam-transport line. A debuncher of 2.1 MV is placed at a position of 20 m from the entrance of the beam-transport line. The peak current of 180 mA is assumed. The number of particles is 3200.

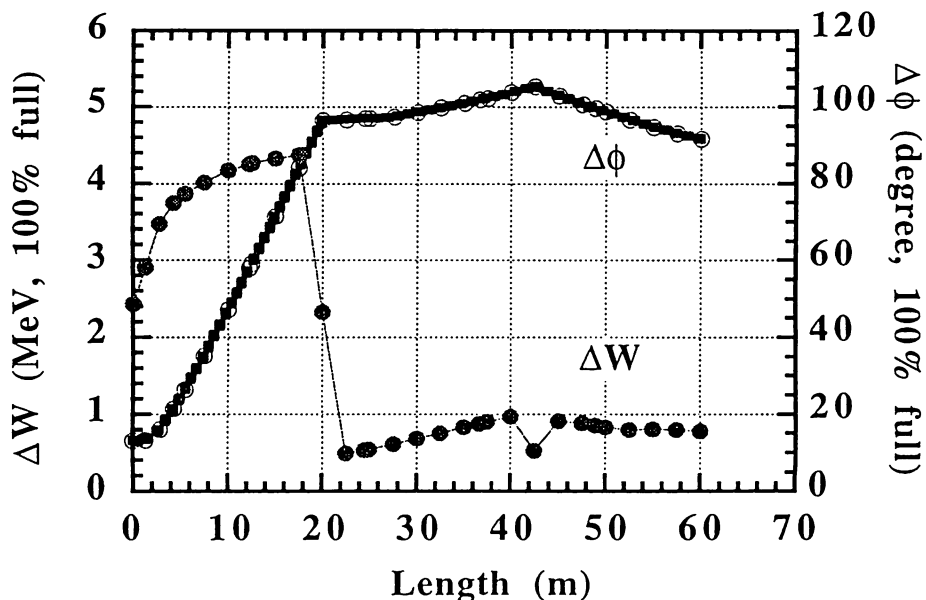


Fig. 4.36 Variation of spreads of phase (in terms of 972 MHz) and energy along the 400-MeV beam-transport line. Two debuncher are used. The voltages are 2.1 and 0.6 MV. They are placed at a position of 20 and 42.5 m from the entrance of the beam-transport line. The peak current of 180 mA is assumed. The number of particles is 3200.

### 4.3.13 Power dividing method for SDTL unit tanks

Figure 4.30 shows the rf driving power, beam power and total power for the unit tanks of the SDTL structures. Because of adopting a rather high accelerating field, the total power required for a unit tank varies from 0.48 to 0.89 MW. Assuming a 3-MW peak power klystron and its best efficiency, the first klystron supplies rf power to the first four successive SDTL tanks. Each of the next three klystrons supplies rf power to three successive SDTL tanks, and each of the other klystrons supplies two successive SDTL tanks. There are two ways to supply rf power into the unit tank. One is to use bridge-couplers between adjacent unit tanks. The other is to use a power divider such as a magic Tee or a 3-dB directional coupler to feed each unit tank. Both the DTL and SDTL structures are driven by  $2\pi$ -mode operation, in which the group velocity is zero. Thus, some devices for stabilizing the structure are required, in particular, under heavy beam-loading operation. For the DTL structure, additional post couplers can stabilize the field. For SDTL structures connected through bridge couplers or driven through power divider, no device for stabilizing the field is perhaps necessary, since each structure includes only several numbers of unit cells.

The bridge couplers for the SDTL tanks are discussed in 4.5.4. It is necessary to determine which is a better choice between a bridge coupler or a power divider. The main differences between the two methods are as follows:

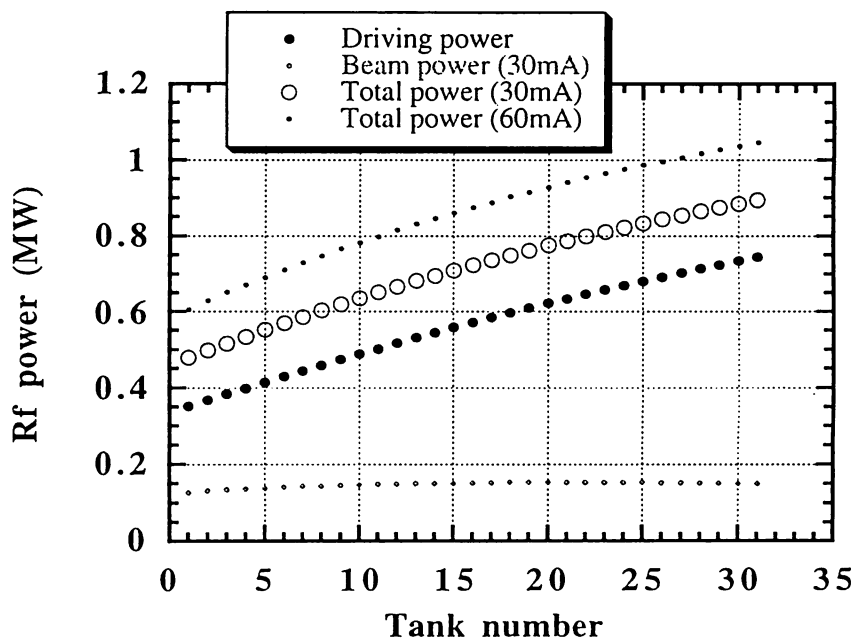


Fig. 4.30 Required rf power for the SDTL tanks. Beam currents of 30 and 60 mA are assumed.

1. Through bridge couplers the field distribution, in both amplitude and phase, is automatically stabilized among connected tanks under any beam loading in the lowest order. (Within each tank there is no stabilizing mechanism as mentioned above.) On the other hand the power divider equally distributes the input power to unit tanks. Since the shunt impedances of the unit tanks are not identical, the field distribution among the unit tanks is slightly deviated from their designed values as discussed below. Also, it is dependent upon the beam current for the same reason.
2. The waveguides connected to the power divider may change their length depending upon the power and ambient temperature, resulting in the variation of the relative phases of the fields.
3. Only one input coupler is necessary for the bridge-coupled system, while the same number of input couplers as that of the connected tanks are necessary for the power-divided system. It is hard to say which system is advantageous, since the power of 3 MW may be at the controversial level regarding the stable operation with a single input coupler, in particular, for an RF pulse as long as several hundreds  $\mu$ s.
4. Additional power dissipation of an order of several percents is inevitable in the bridge coupler because of its standing-wave operation, while the power loss in the power divider or the associated waveguides is much less because of their traveling-wave operation.
5. The bridge coupler for the SDTL is a new device which requires the further study including the fabrication and fundamental operation tests, the high power test, and the long-term operation test, although the conceptual design is completed as described in 4.5.8. On the other hand, the power divider and the associated dummy load are commercially available devices. They are also those easily replaceable, in particular, outside the vacuum system.
6. The cost comparison is not easy, requiring detailed, careful study. In the case of two connected tanks the bridge-coupled system requires one bridge coupler and one input coupler, while the power-divided one requires one power divider, one dummy load, two input couplers and additional waveguide system.

Since the bridge coupler for the SDTL is a new device, the feasibility study concerning the its RF characteristics is necessary. The result is described in 4.5.8, since it is a matter of structure. On the other hand, the disadvantage item 1 above regarding the use of the power divider requires the quantitative study in order to show the feasibility of this choice. Figure 4.31 shows the relative required power ratio for the tanks driven by klystrons. Here, the required rf power is normalized by that for the first tank in each rf dividing set. Since the shunt impedances vary with the energies, the required rf power for each tank driven by a klystron also changes by 14% within the first rf dividing set with four SDTL unit tanks, for example. The required rf power also depends upon the beam loading. Thus, once the rf power is correctly divided according to the required value with zero current, the errors increase as the beam loading increases. Figure 4.32 shows the ratio between the power dividing ratio with zero current and that with 60 mA. In this case, a 2.5%-error in rf power is inevitable among four tanks driven by the first klystrons. In order to reduce this, a smaller num-

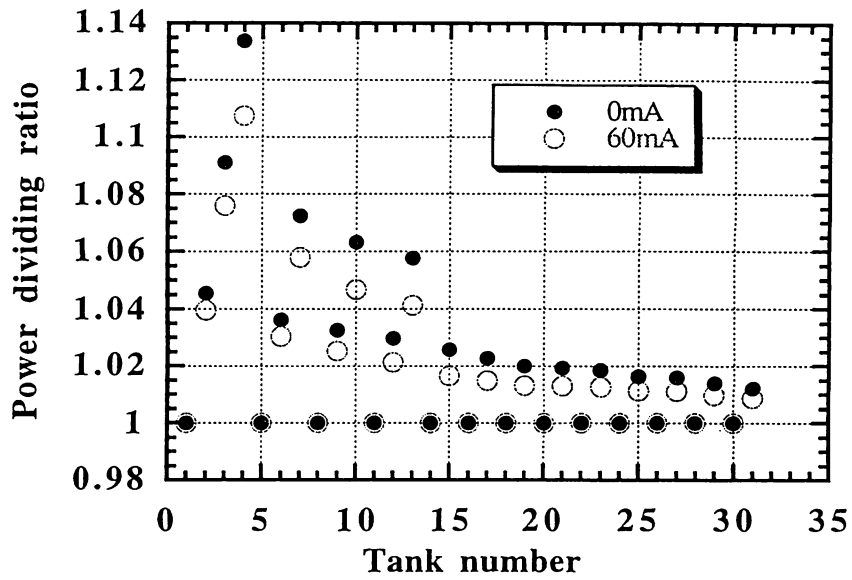


Fig. 4.31 Relative required power ratio among SDTL tanks driven by klystrons of the same amount of an rf output. In the system, there are one four-combined tanks, three three-combined tanks and nine two-combined tanks.

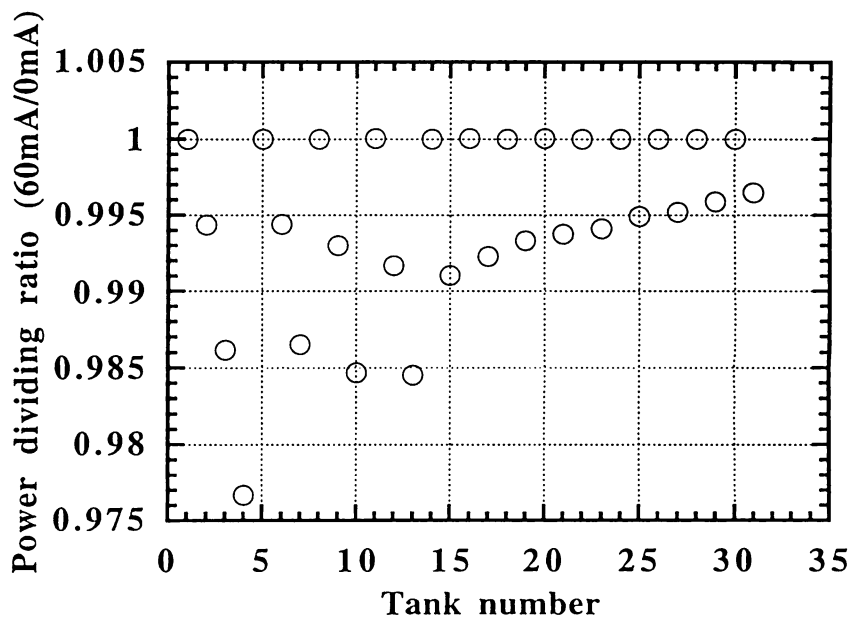


Fig. 4.32 Ratio between the power dividing ratio with zero current and that with 60 mA

ber of power dividing is desirable. In fact, our design assumes 2.5-MW peak-power klystrons, driving three and two tanks. In two-tank case, a field error due to beam loading of 30 mA is less than 0.3% and is within the tolerance determined by beam-loss simulations in the SDDL. From the viewpoint of the total rf system, it is more desirable that all klystrons drive the same number of SDDL tanks. This point should be further investigated from the viewpoint of construction cost and rf efficiency.

Since both the methods seem feasible and neither has any decisive advantage, they will be studied in parallel until any decisive difference is found or until the time of the final decision has come.

### 4.3.14 Upgrade of the output energy

Three upgrade plans up to an output energy of 400 MeV are as follows:

- 1) DTL + SDDL (200 MeV) + ACS (972 MHz),
- 2) DTL + SDDL (200 MeV) + ACS (1296 MHz),
- 3) DTL + SDDL (150 MeV) + ACS (972 MHz).

The first and second plans add a CCL section to the existing linac. The choice of the operating frequency for a CCL depends upon the beam quality at the exit of the 200-MeV linac and the results of beam simulation in the CCL part. The third plan removes a part of the existing linac and adds a CCL of 972-MHz. If a transition energy of around 150 MeV is selected, a frequency multiplication factor of three is recommended according to our simulation results. On the other hand, if a transition energy of 200 MeV is selected, a frequency multiplication factor of four is possible. Here, two plans ((1) and (3)) are summarized in Tables 4.10 to 4.13 and shown in Figs.4.33 and 4.34. Fortunately, we will have a chance to study the properties of an output beam of 200 MeV. Therefore, a final determination of the CCL operating frequency should be put off to the future.

It is needless to say that the optimum coupled-cavity linac structure should be chosen at the time of the upgrade, since new structures may come out by that time. However, we assume the ACS here, since we believe that the ACS is the best choice at present over the side-coupled structure (SCS), the on-axis coupled structure (OCS), and the disc-and-washer structure (DAW). The ACS is the one which has the balanced characteristics of both the shunt impedance and the field symmetry [18].

The transverse electric kick [19] existing in the SCS gives rise to a slight amount of continuous transverse oscillation of the beam core, possibly resulting in halo formation, although we need quantitative study in order to prove this possibility. The effective shunt impedance of the OCS decreases as the energy decreases because of the existence of walls between two adjacent cells and

### JHF 400-MeV PROTON LINAC

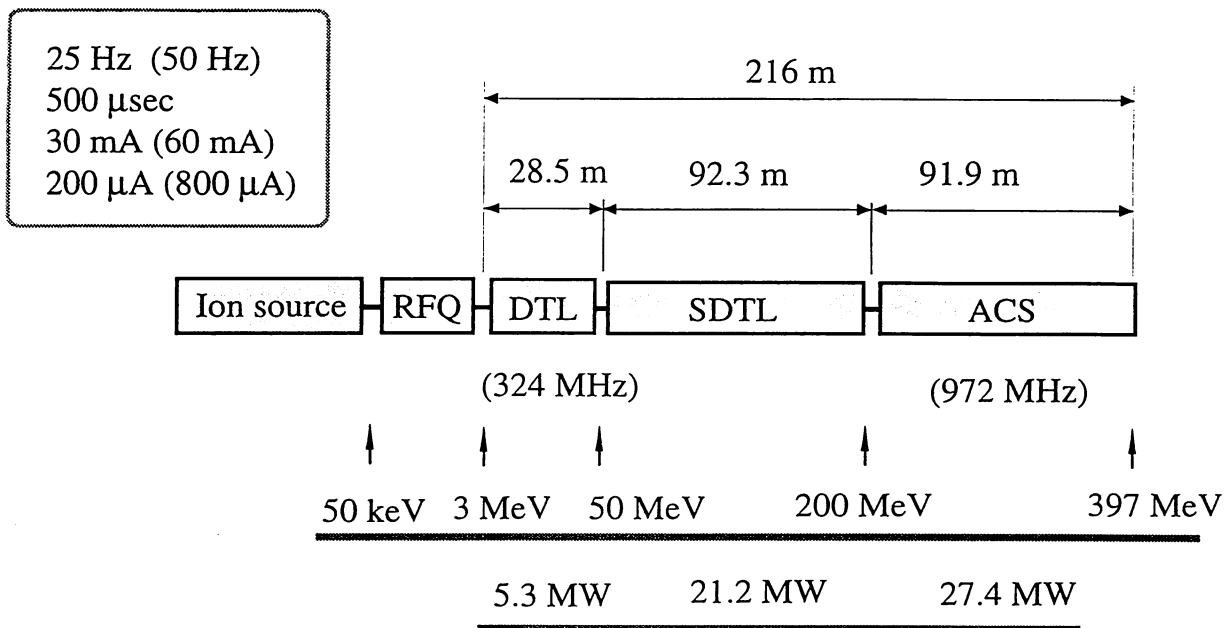


Fig. 4.33 Schematic view of the JHF 400-MeV proton linear accelerator (upgrade plan (1)).

### JHF 400-MeV PROTON LINAC

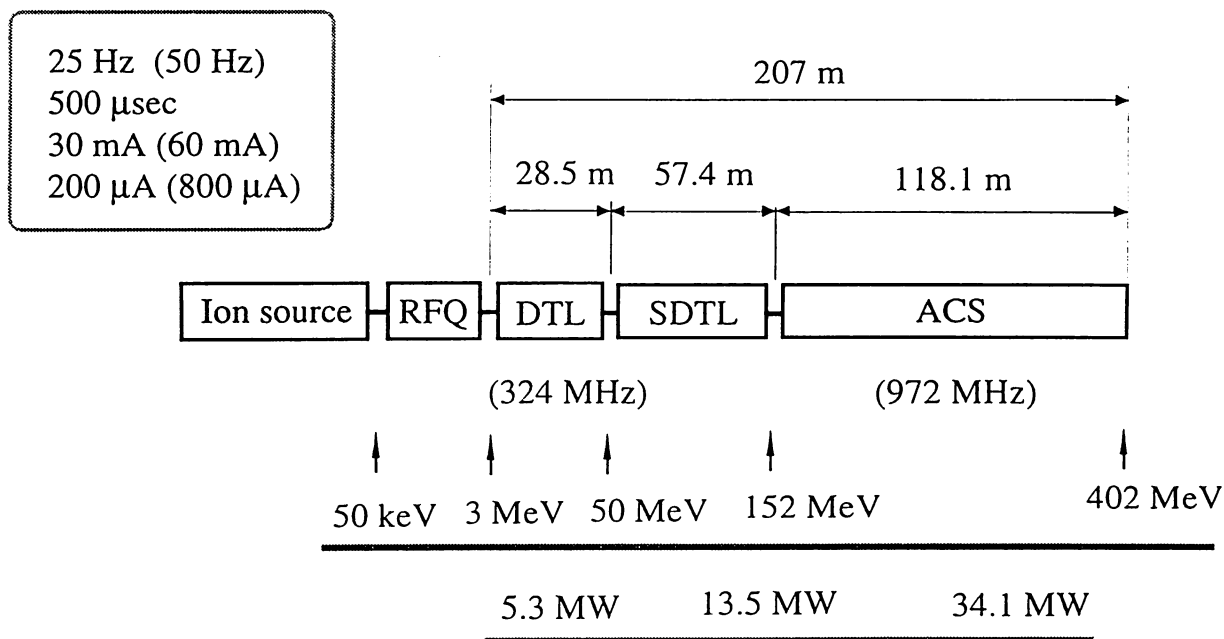


Fig. 4.34 Schematic view of the JHF 400-MeV proton linear accelerator (upgrade plan (3)).

coupling cells on the beam axis. The effect is more serious for a high-duty factor CCL, since the required wall thickness between two adjacent cells for water cooling becomes very large in a low- $\beta$  structure. The DAW, both the shunt impedance and coupling of which are the highest, has still the nearby deflecting mode, which may be mixed to the accelerating mode, if the dipole symmetry is broken. The extensive discussion on the advantage and disadvantage of these structures are presented in ref. 18.

The fundamental RF issues concerning the ACS were already solved and a high-power RF test using the 1296-MHz model cavity was successfully performed [20]. Therefore, the future extension using a 972-MHz ACS will be possible with some efforts of modification.

### 4.3.15 Output beam of the JHF 200-MeV linac

Beam simulation in the JHF 3-MeV, 324-MHz RFQ with more realistic parameters was performed recently [21]. Hereafter, their beam parameters are named as type-RFQ. Figure 4.35 shows rms emittances of three types of DTL injection beam (type-A, type-B and type-RFQ). The transverse emittance of the JHF-RFQ simulation gives intermediate value between type-A and type-B, while the longitudinal one is smaller than the other two (type-A and type-B). Thus, simulation using both type-A and type-RFQ beams of 30 mA were performed. Here, the collision parameter ( $\alpha$ ) was set to 1 and random errors in the accelerating field in the SDTL was taken into account (random errors of  $\pm 2\%$  in an accelerating field for each cell and each tank and random errors of  $\pm 3\%$  in an accelerat-

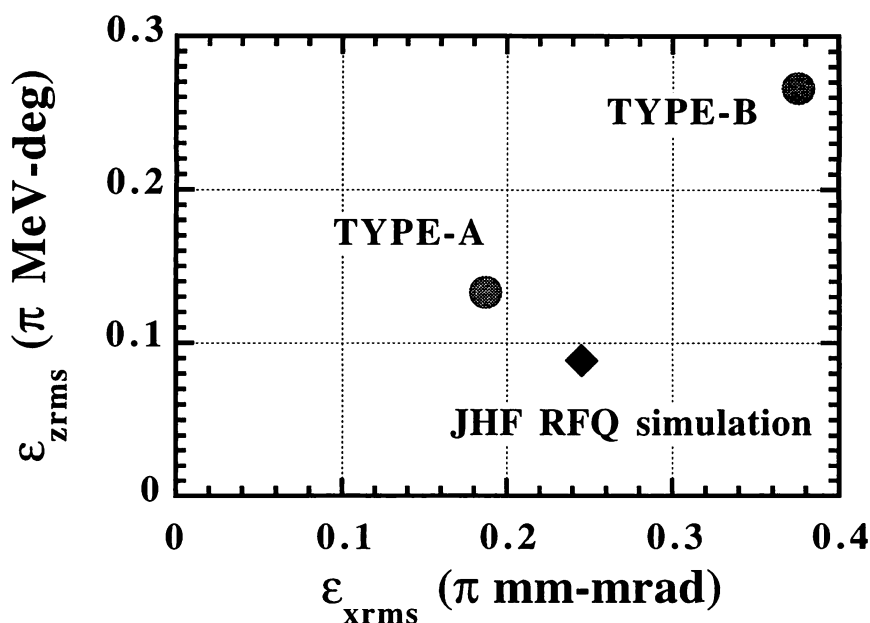


Fig. 4.35 Comparison among rms emittances for three types of DTL injection beams.

ing phase for each tank ). The number of particles in the simulation was 3200. The results are summarized in Table 4.12.

### 4.3.16 Summary

A 200-MeV proton linear accelerator for JHF has been designed. It consists of a 3-MeV radio-frequency quadrupole linac (RFQ), a 50-MeV drift tube linac (DTL) and a 200-MeV separated-type drift tube linac (SDTL). A frequency of 324 MHz has been chosen for all of the rf structures from the viewpoints of the space-charge effects and availability of klystrons. A peak current of 30 mA ( $H^-$  ions) of 500  $\mu$ sec pulse duration will be accelerated at a repetition rate of 25 Hz. A future upgrade plan up to 400 MeV is also presented, in which an annular-coupled structure (ACS) of 972 MHz is used above 150 or 200 MeV. The important features of the design are as follows:

- 1) High performance for beam-loss problem during acceleration can be achieved by adopting an SDTL for a medium energy structure. The space-charge effects in SDTL decreases compared with those in CCL in an accelerator complex (DTL + CCL) with the same transition energy. The longitudinal transition at a rather high-energy range decreases the effects of nonlinear problems related to acceleration in the ACS.
- 2) The coupled envelope equations and the equipartitioning theory are used for the focusing design, resulting in a less amount of emittance growth in longitudinal phase space, compared with that in a constant transverse phase advance focusing, and a smaller ratio of halo formation (section 4.3.8).
- 3) The adoption of the SDTL structure improves both the effective shunt impedance and difficulties in fabricating drift tubes with focusing magnets.
- 4) A beam-transport line between the RFQ and the DTL (MEBT) shows good matching of the beam and high performance of the beam-chopping operation.
- 5) Simple mechanical structures for accelerators are selected.
- 6) Klystrons are used.

Table 4.12 Summary of normalized emittances and energy spread in the JHF 200-MeV linac.

Injection beam	Transverse		Longitudinal	
	Type-A rms / 90% $\pi$ mm-mrad	Type-RFQ rms / 90% $\pi$ mm-mrad	Type-A rms / 90% $\pi$ MeV-deg	Type-RFQ rms / 90% $\pi$ MeV-deg
3-MeV input	0.187 / 0.805	0.248 / 1.06	0.133 / 0.566	0.087 / 0.371
200-MeV output	0.279 / 1.24	0.324 / 1.43	0.274 / 1.18	0.255 / 1.08
99% $\Delta W$ (at 200 MeV)			0.917	0.954 (MeV)

- 7) Acceleration ability for an increase in the peak current up to 60 mA is included.
- 8) Smooth upgrade potentiality up to 400 MeV is considered. The transition energy from SDTL to ACS should be determined by using directly accumulated beam data in the future. There are presently two candidates, 150 and 200 MeV.
- 9) The accurate beam-simulation code on a parallel supercomputer was used for confirming the beam-loss problem during acceleration.

The main parameters for the 200- and 400-MeV designs are summarized in Tables 4.2 in section 4.2.3 and Tables from 4.13 to 4.17 in this section.

## References

- [1] T. Kato, "Design of the JHP 200-MeV Proton Linear Accelerator," KEK report 96-17 (1997).
- [2] M. Kihara, "Outline of the Japanese Hadron Facility," Proc. International Workshop on Hadron Facility Technology, 1987, Los Alamos, LA-11130-C p.67; KEK Preprint 86-106, Y. Yamazaki et al., "The 1 GeV Proton Linac for the Japanese Hadron Facility," Proc. Advanced Hadron Facility Accelerator Design Workshop, 1988, Los Alamos, LA-11432-C p. 80 ; KEK Preprint 87-159, "Report of the design study on the proton linac of the Japanese Hadron Project [I]," JHP-10, KEK Internal 88-8 (1988), "Report of the Design Study on the Proton Linac of the Japanese Hadron Project [II]," JHP-14, KEK Internal 90-16 (1990), Y. Yamazaki and M. Kihara, "Development of the High-Intensity Proton Linac for the Japanese Hadron Project," Proc. 1990 Linac Conf., p.543 (1990), "1-GeV LINAC DESIGN NOTE" in appendix A.
- [3] T. Kato, "Proposal of a Separated-type Proton Drift Tube Linac for a Medium-Energy Structure," KEK Report 92-10 (1992).
- [4] T. Kato, "Beam Simulation Code Using Accurate Gap Field Distributions in a Drift Tube Linac," Proc. 1994 International Linac Conf., p.523 (1994).
- [5] A. Ueno et al., "Beam Test of the Pre-Injector and the 3-MeV  $H^-$  RFQ with a New Field Stabilization PISL," Proc. 1996 International Linac Conf., p.293 (1996).
- [6] K.R.Crandall, D.P.Rusthoi, TRACE 3-D Documentation, LA-UR-97-886, May, 1997
- [7] T. Weiland, Part. Accel. **17**, 227 (1985).
- [8] LANL code group, PARMILA Documentation, May, 1995.
- [9] T. Kato, "New Design of an RF Beam Chopper," Proc. 7th Symposium on Accelerator Science and Technology, p.288 (1989).
- [10] T. Kato, "Design of Beam-Transport Line between the RFQ and the DTL for the JHP 1-GeV Proton Linac," Proc. 1994 International Linac Conf., p.59 (1994).
- [11] R. A. Jameson, "Beam-Intensity Limitations in Linear Accelerators," IEEE Trans. Nucl. Sci. **NS-28**, 2408 (1981).
- [12] R. A. Jameson, "On Scaling & Optimization of High-intensity Low-beam-loss RF Linacs for Neutron Source Drivers", AIP Conference Proceedings **279** (1993) 969.

- [13] M. Reiser, "Theory and Design of Charged Particle Beams," Section 5, John Willy & Sons, 1994.
- [14] T. Kato, "Beam Halos due to the Collision Effects in a Proton Drift Tube Linac," submitted to Particle accelerators.
- [15] T. P. Wangler, "Space-Charge Limits in Linear Accelerators," LA-8388 (1980), I. Hofmann and J. Struckmeier, "Generalized Three-Dimensional Equations for the Emittance and Field Energy of High-Current Beams in Periodic Focusing Structures," Part. Accel., **21**, 69 (1987), M. Reiser and N. Brown, "Thermal Distribution of Relativistic Particle Beams with Space Charge," Phys. Rev. Letters, **71**, 2911 (1993), T. P. Wangler et al., "Relation Between Field Energy and RMS Emittance in Intense Particle Beams," IEEE Trans. Nucl. Sci. **32**, 2196 (1985), T. P. Wangler, K. R. Crandall and R. S. Mills, "Emittance Growth from Charge Density Changes in High-Current Beams," AIP Conf. Proc. **152**, 166 (1986), T. P. Wangler, F. W. Guy and I. Hofmann, "The Influence of Equipartitioning on the Emittance of Intense Charged-Particle Beams," Proc. 1986 Linear Accelerator Conf., p. 340 (1986).
- [16] R. L. Gluckstern, "Survey of Halo Formation Studies in High Intensity Proton Linacs," Proc. 1994 International Linac Conf., Tsukuba, Japan, p.333.
- [17] F. Naito et al., "Rf Characteristics of a High-Power Model of the 432 MHz DTL," Proc. 1994 International Linac Conf., p.137 (1992).
- [18] Y. Yamazaki, "Recent Technological Development of Accelerating Structures," Proc. 1992 Linear Accel. Conf., p.580 (1992)
- [19] T. Kageyama et al., "Development of Annular Coupled Structure," Proc. 1992 Linear Accel. Conf., p.456 (1992)
- [20] T. Kageyama et al., "Development of Annular Coupled Structure," Proc. 1994 International Linac Conf., p. 248 (1994).
- [21] A. Ueno, private communication.

Authors of Sections from 4.1 to 4.3

Takao Kato

5. Ka

Authors of Section 4.3.4

Fu Shinian and Takao Kato

Main contributors to Sections from 4.1 to 4.3

Akira Ueno

Eiichi Takasaki

Fujio Naito

Tatsuya Kageyama

Yoshishige Yamazaki

Table 4.13 Parameters of the JHF 400-MeV proton linac (upgrade version).

## Plan-1 RFQ + DTL(50 MeV) + SDDL (200 MeV) + ACS (397 MeV)

Injection energy	3.0 MeV
Output energy	397.3 MeV
Frequency (RFQ, DTL, SDDL)	324 MHz
Frequency (ACS)	972 MHz
Total length (structure only)	154.6 m
Total length (including drift space)	215.9 m
Total rf driving power	42.2 MW
Beam power (30 mA)	11.8 MW
Beam power (60 mA)	23.7 MW
Total rf power (30 mA)	54.0 MW
Total rf power (60 mA)	65.8 MW

## Plan-3 RFQ + DTL(50 MeV) + SDDL (152 MeV) + ACS (402 MeV)

Injection energy	3.0 MeV
Output energy	401.6 MeV
Frequency (RFQ, DTL, SDDL)	324 MHz
Frequency (ACS)	972 MHz
Total length (structure only)	150.9 m
Total length (including drift space)	207.3 m
Total rf driving power	41.0 MW
Beam power (30 mA)	12.0 MW
Beam power (60 mA)	23.9 MW
Total rf power (30 mA)	53.0 MW
Total rf power (60 mA)	64.9 MW

Table 4.14 Parameters of the high-energy part from 149 to 402 MeV with ACS structure.

Frequency	972	MHz
Injection energy	151.6	MeV
Output energy	401.6	MeV
Number of tank	48	
number of cells	872	
Structure length	83.0	m
Total length	118.1	m
Rf driving power (*)	26.6	MW
Beam power (30mA)	7.5	MW
Beam power (60mA)	15.0	MW
Total power (30mA)	34.1	MW
Total power (60mA)	41.6	MW
Accelerating field	4.0 - 4.6	MV/m
Energy gain	2.7 - 3.1	MeV/m
Drift space (**)	0.71 - 0.82	m

(\*) including a factor of 1.2.

(\*\*) shorter length is possible.

Table 4.15 Parameters of the high-energy part from 200 to 397 MeV with ACS structure.

Frequency	972	MHz
Injection energy	200.0	MeV
Output energy	397.3	MeV
Number of tank	36	
number of cells	624	
Structure length	61.8	m
Total length	91.9	m
Rf driving power (*)	21.5	MW
Beam power (30mA)	5.9	MW
Beam power (60mA)	11.8	MW
Total power (30mA)	27.4	MW
Total power (60mA)	33.3	MW
Accelerating field	4.4 - 4.8	MV/m
Energy gain	3.0 - 3.3	MeV/m
Drift space (**)	0.77 - 0.98	m

(\*) including a factor of 1.2.

(\*\*) shorter length is possible.

Table 4.16 Parameters of the SDTL part from 50 to 149 MeV.

Frequency	324	MHz
Injection energy	50.1	MeV
Output energy	151.6	MeV
Number of tank	21	
number of cells	105	
Structure length	40.9	m
Total length	57.4	m
Rf driving power (*)	10.4	MW
Beam power (30mA)	3.0	MW
Beam power (60mA)	6.1	MW
Total power (30mA)	13.5	MW
Total power (60mA)	16.5	MW
Number of klystron	6	
Accelerating field	3.86 - 3.76	MV/m
Energy gain	2.86 - 2.13	MeV/m
Drift space (**)	0.67-0.97	m

(\*) including a factor of 1.2.

(\*\*) shorter length is possible.

Table 4.17 Parameters of the JHF 200-MeV proton linac.

	Injection energy	3.0	MeV
	Output energy	200.0	MeV
	Frequency	324	MHz
	Particles	$H^-$	
	Peak current	30	mA
	Beam width	500	$\mu$ sec
	Repetition rate	25	Hz
	Average current	200	$\mu$ A
	chopping ratio	$\sim 0.56$	
	Total length (structure only)	92.9	m
	Total length (including drift space)	122.2	m
	Total rf driving power	20.6	MW
	Total rf power (30 mA)	26.6	MW
	Total rf power (60 mA)	32.5	MW
	Number of klystrons(*)	19	
	(*)includes for RFQ and debuncher		
RFQ	Frequency	324	MHz
	Injection energy	50	keV
	Output energy	3	MeV
DTL	Frequency	324	MHz
	Injection energy	3	MeV
	Output energy	50.1	MeV
	Number of tank	3	
	number of cells	150	
	Total length	28.51	m
	Rf driving power (*)	3.92	MW
	Beam power (30mA)	1.41	MW
	Beam power (60mA)	2.82	MW
	Total power (30mA)	5.33	MW
	Total power (60mA)	6.74	MW
	Number of klystron	3	
	Acceptance		
	$A_x$ (normalized 90%)	43	$\pi$ mm-mrad
	$A_y$ (normalized 90%)	41	$\pi$ mm-mrad
	$A_z$ (normalized 90%)	9.3	$\pi$ MeV-deg
	Focusing method	Equipartitioned focusing	
	Stabilization	Post-stabilized	

DTL Tank number	1	2	3	
Injection energy	3.0	19.196	35.407	MeV
Output energy	19.196	35.407	50.058	MeV
Tank length	10.36	8.87	7.81	m
Number of cells	80	41	29	
Rf driving power (*)	1.16	1.36	1.40	MW
Beam power (30mA)	0.49	0.49	0.44	MW
Beam power (60mA)	0.98	0.98	0.88	MW
Total power (30mA)	1.64	1.84	1.84	MW
Total power (60mA)	2.08	2.33	2.28	MW
Accelerating field	2.5	2.7	2.9	MV/m
Stable phase	-30	-26	-26	
Drift space	4	3	0	$\beta\lambda$
	0.737	0.742		m

(\*) including a factor of 1.3

#### SDTL

Frequency	324	MHz
Injection energy	50.058	MeV
Output energy	200.022	MeV
Number of tank	31	
number of cells	155	
Structure length	65.8	m
Total length	92.3	m
Rf driving power (*)	16.7	MW
Beam power (30mA)	4.5	MW
Beam power (60mA)	9.0	MW
Total power (30mA)	21.2	MW
Total power (60mA)	25.7	MW
Number of klystron	14	
Accelerating field	3.86 - 3.60	MV/m
Energy gain	2.86 - 1.80	MeV/m
Drift space (**)	0.67-1.03	m
Acceptance		
$A_x$ (normalized 90%)	21.3	$\pi$ mm-mrad
$A_y$ (normalized 90%)	18.6	$\pi$ mm-mrad
$A_z$ (normalized 90%)	40.4	$\pi$ MeV-deg

(\*) including a factor of 1.2.

(\*\*) shorter length is possible.